Fast and reliable prediction of scramjet flowfields via Gaussian process latent variable model and deep learning

Fujio, Chihiro
Department of Aeronautics and Astronautics, Kyushu University

Akiyama, Kento
Department of Aeronautics and Astronautics, Kyushu University

Ogawa, Hideaki
Department of Aeronautics and Astronautics, Kyushu University

出版情報：Physics of Fluids. 35, pp.046120-, 2023-04-28. AIP Publishing
バージョン：

Physics of Fluids

RESEARCH ARTICLE | APRIL 28 2023

Fast and reliable prediction of scramjet flowfields via Gaussian process latent variable model and deep learning

Fujio Chihiro (藤尾 秩寛) ; Akiyama Kento (秋山 健人); Ogawa Hideaki (小川 秀朗)

Physics of Fluids 35, 046120 (2023)
https://doi.org/10.1063/5.0148974
CHORUS

Physics of Fluids ARTICLE scitation.org/journal/phf

Fast and reliable prediction of scramjet flowfields via Gaussian process latent variable model and deep learning

Cite as: Phys. Fluids **35**, 046120 (2023); doi: 10.1063/5.0148974
Submitted: 3 March 2023 · Accepted: 11 April 2023 ·
Published Online: 28 April 2023

Chihiro Fujio (藤尾 秩寛), Kento Akiyama (秋山 健人), and Hideaki Ogawa (小川 秀朗)[a)]

AFFILIATIONS

Department of Aeronautics and Astronautics, Kyushu University, 744 Motooka, Nishi-ku, Fukuoka, Fukuoka 819-0395, Japan

[a)]Author to whom correspondence should be addressed: hideaki.ogawa@aero.kyushu-u.ac.jp

ABSTRACT

Fast and accurate prediction of high-speed flowfields is of particular interest to researchers in fluid science and engineering to enable efficient design exploration and knowledge discovery. The reliability of prediction is another important metric for the performance of prediction models. While predictive modeling approaches with and without reduced-order modeling (ROM) via machine learning techniques have been proposed, they are inherently subject to loss of information for ROM-based approaches and substantial computational costs in modeling for non-ROM-based approaches. This paper proposes an accurate ROM-based predictive framework with minimum information loss enabled by incorporating Gaussian process latent variable modeling (GPLVM) and deep learning. The stochastic nature of GPLVM allows for uncertainty quantification that indicates the degree of prediction error or reliability of prediction without requiring validation data. The applicability for supersonic/hypersonic viscous flowfields has been examined for two cases including axisymmetric intakes and two-dimensional fuel injection in scramjet engines by comparison with other predictive models. Comparable or superior prediction accuracy over the other models has been achieved by the proposed approaches, demonstrating its high potential to serve as a new competent, data-driven technique for fast, accurate, and reliable prediction of scramjet flowfields.

NOMENCLATURE

CFD	Computational fluid dynamics
CNN	Convolutional neural network
DMD	Dynamic mode decomposition
GPLVM	Gaussian process latent variable model/modeling
MAE	Mean absolute error
MAPE	Mean absolute percentage error
MLP	Multilayer perceptron
POD	Proper orthogonal decomposition
RBF	Radial basis function
RMSE	Root mean squared error
RMSPE	Root mean squared percentage error
ROM	Reduced-order model/modeling
UQ	Uncertainty quantification

I. INTRODUCTION

Supersonic combustion ramjet (scramjet) engines draw attention as a promising propulsion technology for hypersonic atmospheric flights in high-speed point-to-point transportation as well as access-to-space transportation. As a class of airbreathing propulsion, scramjets are beneficial in terms of efficiency, maneuverability, and safety.[1] To enable space transportation, they need to be employed in combination with other propulsion systems as combined cycles, e.g., rocket-based and turbine-based combined cycles (RBCC and TBCC, respectively) due to lack of propulsive ability outside the hypersonic regime. A feasibility study of RBCC-based space transportation systems has revealed their advantages over conventional systems using only rocket engines in the case of two-stage-to-orbit (TSTO).[2] Scramjet research and technological development have been conducted since the 1940s and reached a technological level where notable milestones have been marked such as the first successful in-flight supersonic combustion in the HyShot program[3] and the world's fastest flight at a Mach number of 9.68 by X-43A in the Hyper-X program.[1] Toward further development and utilization of scramjet engines, researchers and engineers endeavor to advance methodologies for effective design and knowledge discovery from the viewpoints of both design and physics.

Various approaches have been proposed and employed for designing scramjet engines and their components (e.g., intake, fuel injector, combustor, and nozzle). Analytical and numerical techniques are commonly employed in conjunction with mathematical algorithms or empirical approaches. Design optimization is a capable alternative for both design exploration and knowledge discovery. Multi-objective design optimization studies have been conducted via evolutionary algorithms for scramjet intakes,[4–6] fuel injectors,[7,8] combustors,[9,10] and nozzles.[11,12] Fujio and Ogawa have conducted data mining for the outputs of intake design optimization to reveal the physical rationales that account for the optimality of the resultant design.[13] These studies, which would otherwise be difficult due to substantial costs for computational fluid dynamics (CFD) simulations, have been realized by employing machine learning techniques including surrogate modeling, which can replace CFD simulations with predictions from machine learning. While surrogate models allow for prompt assessments of performance with respect to design criteria of interest, they do not provide direct insight into the rationales behind the results obtained from physics and engineering perspectives. This limitation has motivated researchers to develop new approaches that can retain and provide detailed physical information comparable to that from CFD simulations.

Fast prediction of flowfields is a promising approach to enable low-cost yet high-fidelity assessments in design exploration and knowledge discovery in fluid science and engineering.[14] Predictive modeling approaches can be classified into two groups, depending on the involvement of reduced-order modeling (ROM) techniques in the approach, namely, ROM-based and non-ROM-based approaches. ROM is a dimensionality reduction technique to extract meaningful features and patterns from flowfield data as low-dimensional representations while the flowfield data are recognized as high-dimensional data. Mode decomposition techniques such as proper orthogonal decomposition (POD)[15] and dynamic mode decomposition (DMD)[16] are often employed for the ROM of flowfield data. Comprehensive reviews of these techniques in fluid dynamics are provided by Taira *et al.*[17] and Rowley and Dawson,[18] and studies on their usage and applications have also been reviewed by Taira *et al.*[19] These ROM techniques have been adopted for the construction or prediction of flowfields based on reduced information. Bui-Thanh *et al.* employed gappy POD to construct compressible flowfields over airfoil based on surface pressure distributions.[20] Mifsud *et al.* reported a predictive framework that combines POD and linear regression to predict high-speed external flowfields.[21] Other studies have conducted prediction of high-fidelity flowfields based on simplified or low-fidelity flowfields obtained via numerical simulations.[22,23] While these studies yielded accurate construction of high-fidelity flowfield data, a large number of training data were commonly required. For high-speed internal flowfields, Sun *et al.* employed POD and radial basis function (RBF) to predict inflow-dependent ramjet inlet flowfields characterized by curved shock waves and shock/boundary-layer interaction.[24] The study reported the difficulty in predicting shock trains and separation shock waves while demonstrating the applicability of the RBF-POD predictive framework for such flowfields. Brahmachary *et al.* performed the prediction of scramjet intake flowfields for various shapes employing a similar predictive approach, also reporting the difficulty in predicting shock waves.[25] Such difficulties can be attributed to the fact that conventional ROM techniques employed in these studies discard the information in lower modes because what they solve are not ROM problems but decomposition problems. Another potential factor of the difficulty is that these approaches rely on linear superimposition of modes in prediction or reconstruction of flowfields despite highly nonlinear variations in physical properties associated with complex phenomena such as shock waves. Therefore, accurate ROM techniques that can resolve and represent nonlinear behavior are required to improve the prediction performance of ROM-based predictive frameworks.

Non-ROM-based predictive approaches often employ deep-learning techniques that are capable of predicting highly nonlinear and discontinuous distributions. Fujio and Ogawa employed a deep-learning model for the prediction of scramjet intake flowfields by using design variables as inputs.[26] Accurate prediction of flowfields in the presence of shock waves was achieved owing to the flexible fitting capability of deep learning, while the cost of model training was relatively high even with the acceleration using graphics processing units (GPUs). The predictive approach has been employed for the prediction of fuel injection flowfields inside a scramjet combustor too.[27] Convolutional neural networks (CNNs) have also been employed for the prediction or reconstruction of scramjet flowfields. Kong *et al.* employed a CNN to predict velocity fields based on wall pressure profiles,[28] and Chen *et al.* employed it to reconstruct scramjet combustor flowfields to enable real-time monitoring.[29] Similar studies have been conducted by using various deep-learning techniques,[30,31] and Li *et al.* summarized the recent progress in deep-learning techniques for flow prediction and control.[32] Non-ROM-based models, in particular deep-learning-based models, feature high accuracy even for complicated flowfields that would require larger computational costs for training, whereas ROM-based models are characterized by high computational efficiency with reasonable accuracy. High accuracy comparable to that of deep-learning models and low computational cost comparable to ROM-based models represent the ideal balance for the objective of predictive modeling using state-of-the-art machine-learning techniques.

In addition to computational efficiency and prediction accuracy, the reliability of prediction is another important criterion for the utilization of predictive modeling. Uncertainty quantification (UQ) provides a means to assess the reliability of flow predictions without additional true evaluation (i.e., CFD simulation) of flowfields. Despite considerable benefits of knowing the reliability of the prediction prior to using the prediction outputs, few studies have conducted uncertainty quantification of flow prediction. Qiu *et al.* have employed a model incorporating CNN into the Bayesian theory to perform both prediction and uncertainty quantification.[33] Fujio and Ogawa employed an ensemble-based method with Monte Carlo Dropout and a distance-based method for deep-learning prediction, and the results of the former approach indicated the difficulty in predicting boundary-layer separations caused by shock interactions despite the significant additional computational cost it required.[26] Another notable advantage of UQ is that it provides useful insight into the error distributions for the improvement of model performance. Thuerey *et al.* discussed the importance of comprehension of the sources of prediction errors to improve the model prediction accuracy.[34] Therefore, the prediction model that is capable of quantifying the prediction uncertainty can assure reliable use of prediction.

A nonlinear ROM technique, Gaussian process latent variable model (GPLVM), also attracts attention of researchers. While POD is

a linear ROM technique, GPLVM acquires the capability of nonlinear ROM by introducing nonlinear kernel functions and the assumption of Gaussian distributions, and it is thus known as probabilistic kernel principal component analysis.[35] Reduced-order modeling is performed by mapping the multi-dimensional data onto a latent variable space, where the dimensions of the latent variable vectors can be determined by the users. Nakaya *et al.* employed GPLVM to investigate transient dynamics of hydrogen combustion by analyzing the latent variables.[36] Nishimoto *et al.* employed an extension of GPLVM called shared GPLVM to investigate the effect of penetration height on flame stability in supersonic combustion.[37] These studies have shown that the latent variables obtained via GPLVM can well represent the physical characteristics of the original data. These studies demonstrate the prominent capability of GPLVM as a ROM technique, but it has not been employed for predictive frameworks of flowfields. Further to the notable performance of GPVLM for dimensionality reduction, GPLVM is capable of quantifying the uncertainty in reconstruction from the latent variables to the original data. This is another desirable characteristic that promotes employment of GPLVM in frameworks of flowfield prediction.

The present study proposes a ROM-based predictive framework that employs Gaussian process latent variable models as the ROM technique and deep learning as the predictive capability, aiming to realize fast, accurate, and reliable prediction of flowfields inside scramjet engines. The prediction model is capable of estimation of prediction uncertainty owing to the stochastic characteristics of GPLVM. Case studies are conducted for axisymmetric scramjet intake flowfields and two-dimensional fuel injection flowfields to verify the applicability and to investigate the characteristics of the predictive framework. The performance is examined by comparison with the POD-based and deep-learning-based prediction models, which were previously proposed to predict supersonic/hypersonic flowfields.[25,26] Uncertainty quantification is also performed to assess the potential prediction errors. The selection of kernels and characteristics of the proposed framework are discussed to enhance its applicability and capability in the end.

II. METHODOLOGIES

A. Reduced-order-modeling-based predictive framework

The present study proposes a reduced-order-modeling-based predictive framework for fast, accurate, and reliable prediction of supersonic/hypersonic flowfields. Gaussian process latent variable modeling (GPLVM) is employed for dimensionality reduction and combined with a deep learning method, in particular, multilayer perceptron (MLP) to impart the capability of prediction. GPLVM is a nonlinear ROM technique that suitably serves for the purpose of this because of minimum loss of information in dimensionality reduction incurred in the training process. In addition, GPLVM allows for assessment of uncertainty of the data reconstruction because it is a stochastic process that provides the outputs in the form of probability. The dataset of flowfields is compressed into sets represented by latent variables, which are fed to reconstruct flowfields. A regression model is thus employed to predict sets of latent variables by using the design variables as the inputs. The overview of the present model is schematically shown in Fig. 1. Due to the difficulty in comprehending the distributions and characteristics of latent variables, a deep learning model is employed to associate the latent variables (targets) with the design variables (inputs) so as to allow for flexible fitting without preliminary knowledge of the relation between targets and features. The framework yields a model that predicts one flow variable and multiple models are thus generated to predict multiple variables of flowfields.

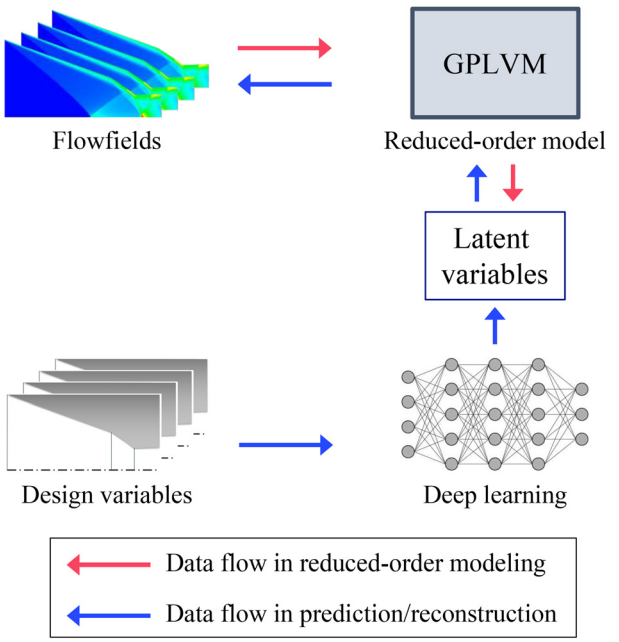

FIG. 1. Schematic of ROM-based predictive framework using GPLVM and deep learning.

1. Gaussian process latent variable modeling

Gaussian process latent variable modeling is a nonlinear ROM technique using a Gaussian process and known as an unsupervised Gaussian process.[35] While other ROM techniques such as POD and DMD perform dimensionality reduction by solving mode decomposition problems and discarding lower modes, GPLVM solves the dimensionality reduction problems themselves with a specified number of latent variables. This effectively allows GPLVM to minimize the loss of data in reduced-order modeling, in contrast to other ROM methods, which inevitably incur some losses in the information of the dataset. The posterior probability of the targets $\mathbf{Y}$ for given latent variables $\mathbf{Z}$ is expressed as

$$p(\mathbf{Y}|\mathbf{Z}) = \prod_{d=1}^{D} \mathcal{N}\left(\mathbf{y}^{(d)}|\mathbf{0}, \mathbf{K}_\mathbf{z}\right), \tag{1}$$

where $\mathcal{N}$ is a multivariate Gaussian distribution, D is the dimensionality of data, $\mathbf{Y}$ and $\mathbf{y}^{(d)}$ represent a matrix of target data and the d^{th} column, respectively. Therefore, $\mathbf{Y}$ and $\mathbf{y}^{(d)}$ are a matrix of flowfield data and the d^{th} flowfield data in the present study. Z is the matrix of latent variables and $\mathbf{K}_\mathbf{z}$ is a kernel matrix.

Reconstruction and prediction of flowfields are performed by feeding a set of latent variables, and GPLVM provides the predicted probability distribution of the target as follows:

TABLE I. Kernel functions considered in the present study.

Name	Definition
RBF	$k(\mathbf{x},\mathbf{x}') = \theta_0 \exp\left(\frac{\lvert\mathbf{x}-\mathbf{x}'\rvert}{\theta}\right)$
Matern52	$k(\mathbf{x},\mathbf{x}') = \theta_0\left(1+\frac{\sqrt{5}\lvert\mathbf{x}-\mathbf{x}'\rvert}{\theta}+\frac{5\lvert\mathbf{x}-\mathbf{x}'\rvert^2}{\theta^2}\right)\exp\left(-\frac{\sqrt{5}\lvert\mathbf{x}-\mathbf{x}'\rvert}{\theta}\right)$
Matern32	$k(\mathbf{x},\mathbf{x}') = \theta_0\left(1+\frac{\sqrt{3}\lvert\mathbf{x}-\mathbf{x}'\rvert}{\theta}\right)\exp\left(-\frac{\sqrt{3}\lvert\mathbf{x}-\mathbf{x}'\rvert}{\theta}\right)$
Exponential	$k(\mathbf{x},\mathbf{x}') = \theta_0 \exp\left(-\frac{\lvert\mathbf{x}-\mathbf{x}'\rvert}{\theta}\right)$
Linear	$k(\mathbf{x},\mathbf{x}') = \theta_0 \mathbf{x}\mathbf{x}'$

$$p(\mathbf{y}_*|\mathbf{z}_*,\mathbf{Y},\mathbf{Z}) = \mathcal{N}\left(\mathbf{k}_*^T\mathbf{K}_\mathbf{z}^{-1}\mathbf{Y}, k_{**}-\mathbf{k}_*^T\mathbf{K}_\mathbf{z}^{-1}\mathbf{k}_*\right), \tag{2}$$

$$\mathbf{k}_* = (k(\mathbf{z}_*,\mathbf{z}_1), k(\mathbf{z}_*,\mathbf{z}_w),\ldots,k(\mathbf{z}_*,\mathbf{z}_N)), \tag{3}$$

$$k_{**} = k(\mathbf{z}_*,\mathbf{z}_*), \tag{4}$$

where the subscript $*$ denotes the targeted case and N is the number of samples or the size of the dataset. $\mathbf{k}$ represents the kernel function. The expectation and variance of the predicted probability distribution are then regarded as the predicted or reconstructed flowfield and the uncertainty of prediction, respectively. From Eq. (2), the expectation and variance can be expressed as follows:

$$\mathbb{E}(p(\mathbf{Y}|\mathbf{Z})) = \mathbf{k}_*^T\mathbf{K}_\mathbf{z}^{-1}\mathbf{Y}, \tag{5}$$

$$\mathbb{V}(p(\mathbf{Y}|\mathbf{Z})) = k_{**}-\mathbf{k}_*^T\mathbf{K}_\mathbf{z}^{-1}\mathbf{k}_*. \tag{6}$$

Kernel functions indicate the similarity between the dataset and the input data and determine the characteristics of the model. In the present study, five kernel functions summarized in Table I are considered with hyperparameters θ_0 and θ for the ROM of flowfields.

The training of GPLVM is performed to maximize the probability in Eq. (2). Gradient-based optimization minimizes the loss function L_{GP}, which is defined as follows:

$$\begin{aligned} L_{\mathrm{GP}} &= \log\left(p(\mathbf{Y}|\mathbf{Z})\right) \\ &= -\frac{ND}{2}\log(2\pi) - \frac{D}{2}\log|\mathbf{K}_\mathbf{z}| - \frac{1}{2}\mathrm{tr}\left(\mathbf{K}_\mathbf{z}^{-1}\mathbf{Y}\mathbf{Y}^T\right). \end{aligned} \tag{7}$$

Limited memory Broyden–Fletcher–Goldfarb–Shanno (L-BFGS) algorithm[38] is employed, and the modeling and prediction of GPLVM are performed by using a Gaussian process framework GPy.[39]

2. Deep learning

Multilayer perceptron (MLP) is employed for deep learning to predict latent variables from design variables. Deep learning operation is performed by using Tensorflow.[40] The architecture of MLP in the present study is schematically shown in Fig. 2.

The input layer receives a set of design variables as the inputs. Hidden layers then play a role in mapping the inputs to the output space. The numerical process in a hidden layer is expressed as follows:

$$h_j^1 = f\left(w_j^1 x_j + b_j^1\right), \tag{8}$$

$$h_j^l = f\left(\sum_{k=0}^{N^{l-1}} w_{jk}^l h_k^{l-1} + b_j^l\right), \tag{9}$$

where x_j is the jth input, N^{l-1} is the numbers of neurons in the $(l-1)$ th layer, b_j^l is the bias for the jth neuron in the lth layer, and h_j^l is the output from the jth neuron in the lth layer. f represents the activation function, for which rectified linear unit (Relu function) is used in the present study. The numbers of layers and neurons in each layer are determined to be 5 and 1024, respectively, based on a preliminary investigation conducted by the authors.

The training of MLP is performed by minimizing the loss function defined in Eq. (10) via a stochastic gradient descent algorithm Adam (adaptive momentum estimation),[41]

$$L_{\mathrm{MLP}} = \frac{1}{NN_{lv}}\sum_{m=1}^{N}\sum_{n=1}^{N_{lv}}\left(\tilde{y}_{m,n}^* - y_{m,n}^*\right)^2 + \lambda\mathbf{w}^{\mathrm{T}}\mathbf{w}, \tag{10}$$

where N and N_{lv} are the numbers of training data and latent variables, respectively. $\tilde{y}$ and y are the predicted and actual values of target data, and the superscript $*$ represents the standardized properties. The second term in Eq. (10) is a regularization term to mitigate the risk of overfitting. λ is the coefficient that determines the degree of regularization (10^{-5} in the present study), and $\mathbf{w}$ is the matrix composed of the weights and biases of neurons. The training process is iterated for 10 000 epochs with a learning rate of 10^{-5}.

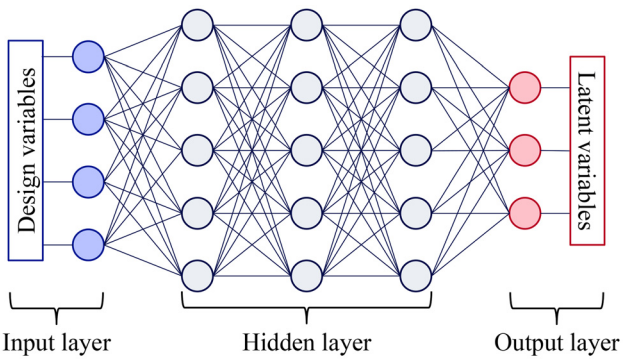

FIG. 2. Schematic of MLP architecture.

TABLE II. Error measurements considered in this study.

Name (abbreviation)	Definition
Mean absolute error (MAE)	$MAE = \frac{1}{N}\sum^{N}\lvert\tilde{y} - y\rvert$
Mean squared error (MSE)	$MSE = \frac{1}{N}\sum^{N}(\tilde{y} - y)^2$
Root mean squared error (RMSE)	$RMSE = \sqrt{\frac{1}{N}\sum^{N}(\tilde{y} - y)^2}$
Mean absolute percentage error (MAPE)	$MAPE = \frac{1}{N}\sum^{N}\frac{\lvert\tilde{y} - y\rvert}{\lvert y\rvert}$
Root mean squared percentage error (RMSPE)	$RMSPE = \sqrt{\frac{1}{N}\sum^{N}\left(\frac{\tilde{y} - y}{y}\right)^2}$

3. Error measurements

Various indicators of prediction errors are considered in this study because error assessment based on a single indicator cannot adequately represent the characteristics and tendencies of prediction errors. The error measurements considered are summarized in Table II. Among these error metrics, the mean absolute error (MAE) is mainly employed because it allows for intuitive understanding of the degree of prediction error.

B. Target configurations

The capability of the present ROM-based predictive framework is assessed through application to two cases, namely, (1) axisymmetric intake flowfields and (2) two-dimensional fuel injection flowfields in a scramjet engine. The intake flowfields are characterized by the large variation in the intake geometry and subsequently the shock structure, whereas the injection flowfields require prediction of the distributions of various chemical species in the mainstream as well as injection plume. The framework yields models that predict static temperature, static pressure, and velocity components individually, and the other flow properties such as Mach number and density can be calculated subordinarily from the predicted variables. Mass fractions of helium (injectant) and oxygen are predicted additionally for injection flowfields.

1. Axisymmetric intake

The present study considers a three-ramp axisymmetric configuration, which was employed in the SCRAMSPACE program.[42] The schematic of the geometry is shown in Fig. 3 with its design parameters. Among the eight design variables, six parameters, namely, θ_1, $\Delta\theta_2$, $\Delta\theta_3$, l_2, l_3, and r_c, are used to determine the intake shape and the ranges of design variables are bounded as shown in Table III to allow for reasonable variations in intake geometries. The intake entrance radius r_i is fixed at 0.075 m to ensure a constant incoming mass flow rate. The remaining design parameter l_1 is determined by the geometric relations of the other parameters.

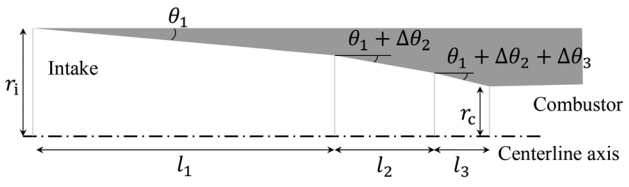

FIG. 3. Schematic of intake geometry and design parameters.

TABLE III. Upper and lower limits of design variables (intake).

Design variable	Unit	Lower limit	Upper limit
θ_1	deg	3.5	6.5
$\Delta\theta_2$	deg	2.5	5.5
$\Delta\theta_3$	deg	0.5	4.0
l_2	m	0.03	0.07
l_3	m	0.01	0.05
r_c	m	0.02	0.04

The operating conditions are calculated assuming a starting point of scramjet operation at an altitude of 30 km on an ascent trajectory with a constant dynamic pressure of 49.7 kPa. The condition is summarized in Table IV. The Reynolds number is calculated by using the intake entrance radius as the reference length.

This configuration was also used as the subject of flow prediction in the other study conducted by the authors[26] and Brahmachary *et al.*[25] The former employed direct prediction via MLP, whereas the latter employed a POD-based predictive framework. These models are employed to be compared with the performance of the present model.

2. Two-dimensional fuel injection

The flowfields caused by two-dimensional fuel injection (Fig. 4) are considered as another subject of the present study. The injection is controlled by its pressure and angle (p_j and α_j, respectively) with their bounds, as summarized in Table V. The inflow conditions are shown

TABLE IV. Freestream conditions (intake).

Altitude (km)	30.0
Mach number M_∞	7.7
Static pressure p_∞ (Pa)	1,197
Static temperature T_∞ (K)	226.5
Reynolds number Re_∞	2.172×10^5

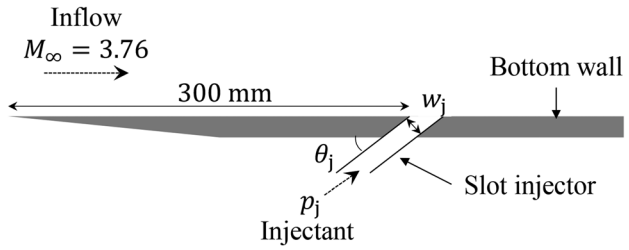

FIG. 4. Schematic of two-dimensional fuel injection and design parameters.

TABLE V. Upper and lower limits of design variables (fuel injection).

Design variable	Unit	Lower limit	Upper limit
p_j	Pa	5.0×10^4	2.0×10^5
α_j	deg	30	90

in Table VI, determined based on the preceding experiment conducted by Inoue *et al.*,[43] and the airflow consists of oxygen and nitrogen with mass fractions of 0.23 and 0.77, respectively. The helium is injected at a sonic speed from the injector for comparison with the experiment. The area of the injector (with the width perpendicular to the direction of injection, w_j) is adjusted according to the injection pressure to ensure a constant mass flow rate of the injectant, i.e., 31.1 kg/(s m), which would yield a fuel/air equivalence ratio of 0.142, if hydrogen were used as the fuel. The Reynolds number based on the distance from the leading edge of the flat plate to the center of the injector slot is 1.81×10^7.

C. Computational fluid dynamics

The steady-state flowfields inside scramjet intakes and around fuel injection are calculated by solving the Reynolds-averaged Navier–Stokes (RANS) equations by utilizing ANSYS Fluent 2021 R1[44] with the shear-stress transport (SST) $k-\omega$ turbulence model proposed by Menter.[45] The flowfields are calculated assuming an ideal, calorically perfect gas with a constant specific heat at constant pressure and a thermal conductivity of 1006.43 J/(kg K) and 0.0242 W/(m K), respectively. The viscosity is calculated via Sutherland's law. The flux computation is performed by using AUSM+ (advection upstream splitting method plus) with second-order spatial accuracy. Spatial discretization is achieved by the Green–Gauss cell-based method. The computational domain is discretized by structured grids generated by an open-source mesh generator Gmsh,[46] which has the capability of mesh generation via scripts. The detailed information on the computational setups and meshes as well as the results of the validation study for each case are presented in Secs. II C 1 and II C 2.

1. Axisymmetric intakes

The dataset of axisymmetric intake flowfields employed in the present study was generated in the preceding study conducted by Fujio and Ogawa,[26] comprising 500 geometries for training and 100 for evaluating the performance for unseen geometries. The intake surface is assumed to be an isothermal wall with a static temperature of 300 K.

TABLE VI. Inflow conditions (fuel injection).

Flow condition	Inflow	Fuel injection
Gas	O_2/N_2	He
Mach number M_∞	3.76	1
Static pressure p_∞ (Pa)	1.3×10^4	···
Static temperature T_∞ (K)	74.4	214
Fuel mass flow rate $\dot{m}_{He}$ [kg/(s · m)]	31.1	0.194
Reynolds number Re_∞	1.81×10^7	···

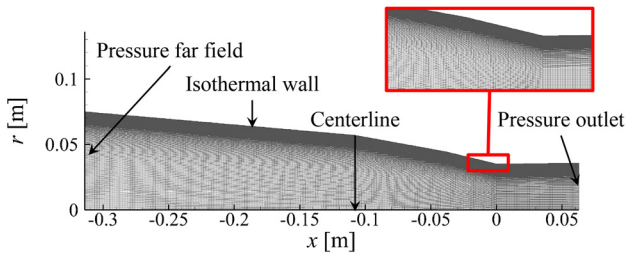

FIG. 5. Computational mesh and boundary conditions (baseline intake geometry, nominal mesh resolution).[26]

Convergence has been ensured for all cases so that the energy residual becomes smaller than 10^{-5} or the residual of mass flow rate decreases within 0.1%. The nominal computational mesh consists of 120 000 cells (301 nodes along the centerline and the intake surface and 401 nodes in the radial direction) and the numbers of cells and nodes in each direction are fixed for all cases. The mesh for the baseline case is displayed in Fig. 5 along with the boundary conditions. The mesh resolution is determined by examining the flowfields and performance with those obtained with the coarse and fine meshes comprising 30 000 and 480 000 cells, respectively. The exit flow profiles are compared in Fig. 6.

The validation study is conducted by comparison with an experimental result for an axisymmetric three-ramp intake conducted in the SCRAMSPACE program.[47] The wall pressure coefficients calculated from the numerical simulation using the computational setups described above are compared with those obtained from shock tunnel testing in Fig. 7. Reasonable agreement can be seen between the CFD and experimental results, verifying the suitability of the present numerical arrangements for axisymmetric three-ramp intakes.

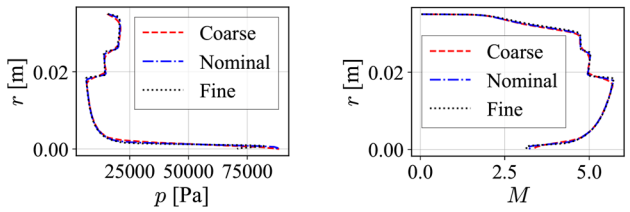

(a) Static pressure (b) Mach number

FIG. 6. Comparison of intake exit flow profiles among meshes with different resolutions.[26]

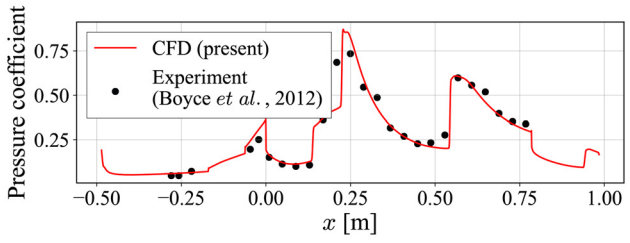

FIG. 7. Comparison of wall pressure coefficient distributions between CFD (present) and experiment[47] (intake).

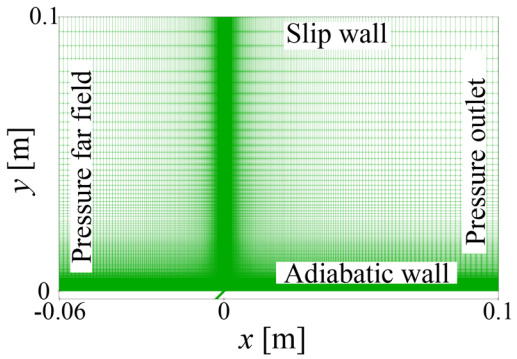

FIG. 8. Computational mesh and boundary conditions (fuel injection, nominal mesh resolution).

2. Two-dimensional fuel injection

The dataset of two-dimensional fuel injection employed in the present study was generated in the preceding study conducted by Akiyama and Ogawa,[27] comprising 300 cases for training and 100 for evaluating the performance for unseen cases. The convergence criterion of the numerical simulations is set to 10^{-3} for the energy residual and 10^{-3} kg/s for the difference in mass flow rate between the inflow (total of mainstream and injection) and outflow. The boundary conditions are depicted in Fig. 8 with the nominal mesh and design parameters. The bottom wall is assumed to be an adiabatic wall and the injection slot is taken to be a slip wall.

A preliminary study has been performed to examine the validity of the numerical modeling as well as to determine a suitable resolution that can adequately resolve the flowfield at reasonable computational cost. The computational meshes consist of 66 280 cells for the coarse resolution, 136 473 cells for the nominal resolution, and 498 830 cells for the fine resolution. Figure 9 displays the wall pressure distributions for each resolution and that of the experimental measurement reported in the preceding work.[43] The pressure distribution with the nominal mesh agrees with that of the fine mesh, indicative of the reasonable resolution provided by the nominal mesh. Based on this analysis, the nominal mesh resolution has been chosen for the present study. The CFD result also agrees with the experimental result, indicating the validity of the numerical setup.

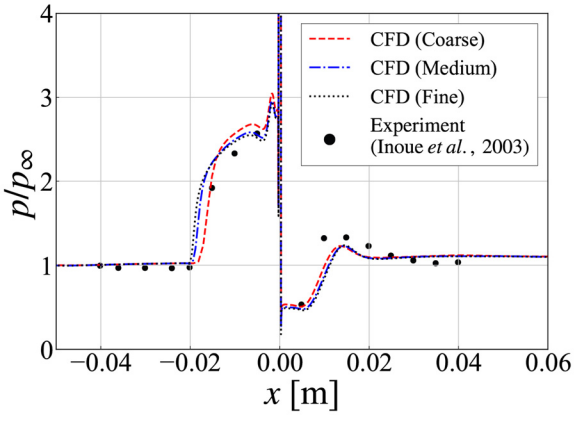

FIG. 9. Comparison of wall pressure distributions from CFD with various mesh resolutions[27] and experiment[43] (fuel injection).

III. RESULTS

A. Axisymmetric intakes

1. Performance of ROM and prediction

The results are discussed for static temperature T first, followed by a summary of the results of the other flow properties, namely static pressure p and axial and radial velocity components u and v, respectively. This is because static temperature distributions represent the effects of both shock waves and boundary layers. The performance of GPLVMs in producing ROM of intake flowfields is evaluated based on reconstruction errors, which are defined as the difference between original flowfields and the flowfields returned from GPLVMs using the actual latent variables as inputs. The average reconstruction errors are compared among GPLVMs with various kernels and POD for static temperature with respect to the number of modes N_m or that of latent variables N_{LV} in Fig. 10. Except for the case of GPLVM with the linear kernel, GPLVMs have achieved more accurate dimensionality reduction than POD. The close overlap between GPLVM with the linear kernel and POD is reasonable because it is known that GPLVM with the linear kernel and automatic relevance determination (ARD) is equivalent to principal component analysis. The difference in the kernel has been found to affect the ROM performance of GPLVM, and the exponential kernel has achieved the minimum reconstruction error among the kernels examined in the present study. While the accuracy of POD increases with the number of modes used for reconstruction, the reconstruction accuracy becomes nearly independent of the number of latent variables in the case of GPLVMs with the exponential and Matern32 kernels when it is larger than 5 and 15, respectively. Although this characteristic of GPLVMs may restrict the maximum accuracy of ROM, these results indicate their capability of effective dimensionality reduction, which is deemed suitable for flow prediction because larger numbers of modes/latent variables may affect the accuracy of the predictive part in the present framework.

The average reconstruction MAE is compared between GPLVM with the exponential kernel and POD for the other flow properties in Fig. 11. The vertical bars represent the standard deviation of the reconstruction MAE. The exponential kernel has been selected for the present study due to its suitability observed in Fig. 10, where the MAEs have been reduced to a reasonably small level at a small number of

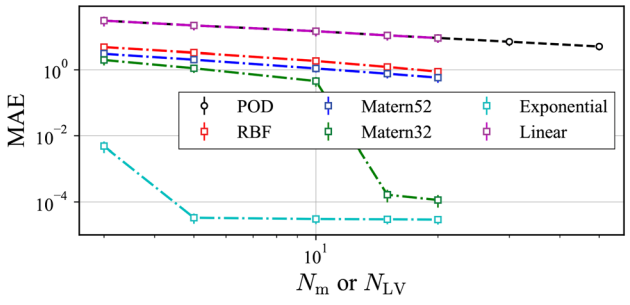

FIG. 10. Comparison of average reconstruction MAEs of static temperature among GPLVMs with different kernels and POD (intake).

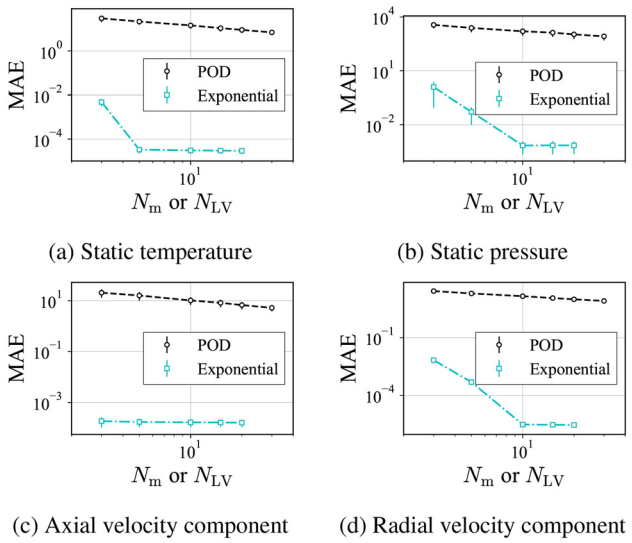

FIG. 11. Comparison of average reconstruction MAEs between GPLVM and POD for other flow properties (intake).

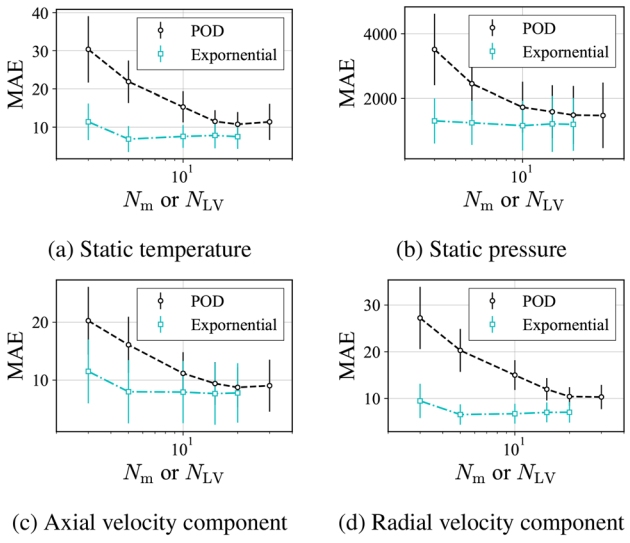

FIG. 13. Comparison of average prediction MAEs between GPLVM and POD for other flow properties (intake).

latent variables, indicative of the superior performance of GPLVM with this kernel, as compared to POD.

The prediction accuracy is compared in Fig. 12. Smaller prediction errors can be observed for GPLVMs than POD for the same number of latent variables/modes except for the cases using the RBF kernel with a larger number of latent variables than 10. The smallest prediction error is achieved in the case of the exponential kernel with five latent variables. The prediction error with POD becomes minimal with a moderate number of modes (20 in the present case) because the reconstruction error decreases with the number of modes whereas the prediction errors increase in the predictive part. This signifies that GPLVM is a more suitable ROM technique for predictive modeling than POD, while POD can reduce the reconstruction error to almost zero by using all modes.

The superiority of the GPLVM-based predictive framework over the POD-based one has further been confirmed by conducting predictive modeling for other flow properties in Fig. 13. Table VII compares the prediction errors between GPVLM with the exponential kernel and POD with respect to various error measurements, indicative of smaller values for GPLVM for all error measurements. The analysis below is conducted by using the most accurate model for each flow property (e.g., GPLVM with five latent variables for static temperature).

Predicted flowfields via GPLVM with the exponential kernel are compared with actual (CFD) flowfields in Fig. 14 and the distributions of absolute error ($E_{\mathrm{abs},T} \equiv |T - \tilde{T}|$) are shown in Fig. 15. The displayed cases have the smallest MAE of static temperature (ID 66), the median MAE (ID 37), and the largest MAE (ID 64), respectively. The ID number is the identifier of each case in dataset. Relatively large prediction errors are observed in the vicinity of shock waves for all cases while the other regions have been predicted accurately. Such prediction errors in shock regions have also been reported in the preceding studies.[25,26] In the predicted flowfield with the largest MAE [Fig. 15(b)], the prediction errors increase downstream where multiple reflected shocks interact. Due to the dependency of the characteristics of prediction error distributions on those of models observed here, the criteria for selection of suitable kernels for supersonic/hypersonic flow prediction are discussed in Sec. IV A. The distributions of absolute errors in the

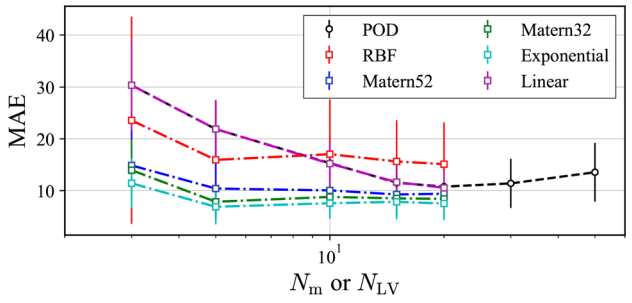

FIG. 12. Comparison of average prediction MAEs of static temperature among GPLVMs with different kernels and POD (intake).

TABLE VII. Comparison of average prediction errors between GPLVM with exponential kernel and POD (intake).

	Model	MAE	MSE	RMSE	MAPE	RMSPE
T	GPLVM	6.88	284.7	15.53	0.010	0.025
	POD	10.77	604.9	23.30	0.018	0.041
p	GPLVM	1155	2.57×10^7	4245	3.54×10^4	4.65×10^7
	POD	1471	4.08×10^7	5170	5.87×10^4	6.46×10^7
u	GPLVM	7.659	534.6	18.00	52.21	1045
	POD	8.737	554.7	19.80	413.1	8271
v	GPLVM	6.54	348	17.9	7627	5.31×10^4
	POD	10.3	704	25.8	5.87×10^4	2.55×10^6

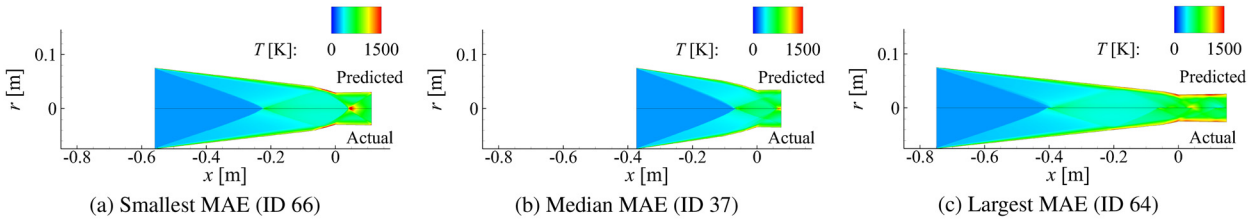

(a) Smallest MAE (ID 66) (b) Median MAE (ID 37) (c) Largest MAE (ID 64)

FIG. 14. Comparison between predicted (GPLVM) and actual (CFD) intake flowfields.

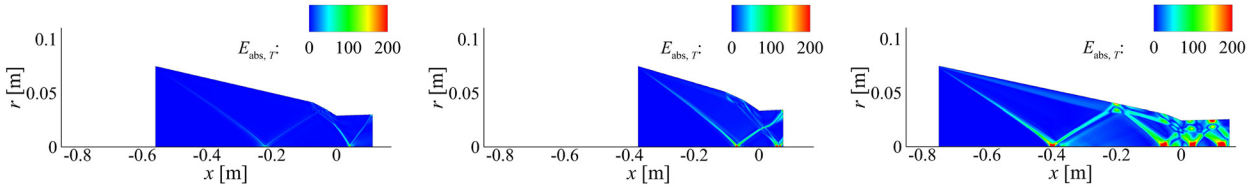

(a) Smallest MAE (ID 66) (b) Median MAE (ID 37) (c) Largest MAE (ID 64)

FIG. 15. Absolute error distributions in intake flowfields for static temperature.

predicted flowfield for ID 37 are displayed in Fig. 16 for the other flow properties. As with the case of static temperature, relatively large prediction errors are present in the vicinity of shock waves.

2. Uncertainty quantification

While POD is a deterministic ROM technique, GPLVM features a stochastic behavior in reconstruction. This enables uncertainty quantification (UQ) by using the variance of reconstruction which is calculated by Eq. (6). The correlation coefficients between the uncertainty in reconstruction and the prediction errors are summarized in Table VIII, with an example shown in Fig. 17 for MAE in static temperature. Strong correlations are observed for most error measurements except for the cases of mean absolute percentage error (MAPE) and RMSPE of static pressure. This potential UQ capability of GPLVM to indicate prediction errors is of particular interest in the practical use of predictive models, as discussed in the preceding study.[26] The present GPLVM-based predictive framework is thus advantageous in terms of not only accuracy but also reliability warranted by its UQ capability.

It is noteworthy that the present UQ only considers the uncertainty in reconstruction (GPVLM part), excluding that in prediction (MLP part). It follows that the uncertainty is determined only by the latent variables. Therefore, it can be considered that the uncertainty in reconstruction implicitly takes the prediction uncertainties of latent variables into account in the form of perturbation or variation from the unknown actual latent variables, i.e., prediction errors of latent variables. Large errors in the predictive part are subsequently reflected on the uncertainty in reconstruction. This has been verified by investigating the relation between uncertainty in reconstruction and perturbation in latent variables in Fig. 18 for static temperature. The perturbation is randomly added within the given maximum percentage differences. An increasing tendency in uncertainty is observed as the perturbation in latent variables increases except for the linear kernel, with which ROM fails to represent the relation between uncertainty and variation in latent variables because of its inadequate accuracy, as seen in Fig. 10. This indicates the importance of the accuracy of ROM for valid UQ.

3. Comparison with direct prediction

The performance and characteristics of the proposed GPLVM-based predictive framework are assessed by comparison with a non-ROM-based model. It is known that MLP is capable of predicting flowfields without involving ROM approaches (thus called *direct prediction* in the present study), as demonstrated in the preceding studies.[26,48] The configurations of the direct prediction model employed for comparison are the same as those used for the predictive part in the present ROM-based approaches. The POD-based approach is also considered for the comparison. For GPLVM-based and POD-based approaches, the models with the minimum averaged MAE have been employed among the models with different numbers of latent variables/modes. The prediction accuracy is compared for various error measurements in Fig. 19 in the relative form of error measurements. GPLVM has resulted in smaller error values than those of direct prediction for all error measurements for static temperature and axial velocity [Figs. 19(a) and 19(c), respectively], whereas direct prediction has produced better performance than the GPLVM model for static pressure and radial velocity [Figs. 19(b) and 19(d), respectively].

The predicted flowfields are assessed by comparing the distributions of static temperature and static pressure on the axis and the intake surface in Figs. 20 and 21, respectively. The direct prediction model has yielded the most accurate prediction for axial distributions of static temperature and static pressure due to its capability to represent nonlinear and discontinuous distributions, as opposed to the results in Fig. 19(a) for static temperature. The comparison of surface distributions of static temperature in Fig. 21(a) indicates that the direct model cannot predict the flowfields near intake surface. The predicted flowfields in the vicinity of the intake surface are compared in Fig. 22. Large averaged prediction errors of static temperature and axial velocity component for the direct model [Figs. 19(a) and 19(c)] can be attributed to

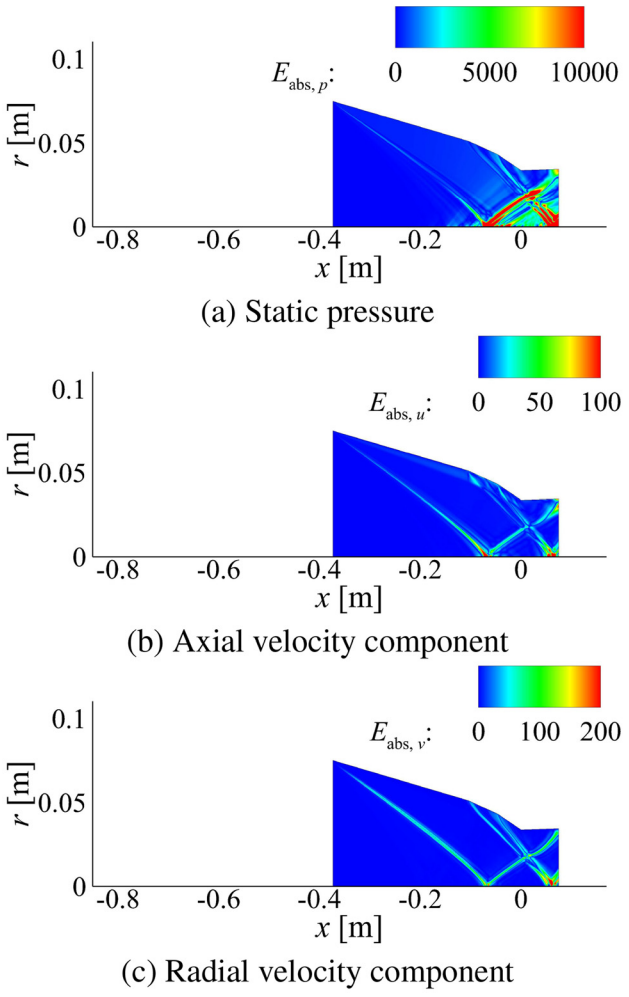

FIG. 16. Absolute error distributions in intake flowfields for other flow properties.

large prediction errors in the vicinity of the intake surface. Further investigation on the characteristics of direct prediction models has not been conducted because it is beyond the scope of the present study.

B. Two-dimensional fuel injection

1. Performance of ROM and prediction

The results for the case of two-dimensional injection flowfields have been assessed with respect to the same metrics as those used for the axisymmetric intakes. In addition to static temperature, helium mass fraction is also investigated mainly due to the importance of species distributions for fuel injection, while the other flow properties (static pressure p, velocity components V_x and V_y, and oxygen mass fraction c_{O_2}) are summarized in a brief manner. While the flowfields consist of three species (i.e., helium, oxygen, and nitrogen), mass fractions of two species (He and O_2) have been predicted because the mass fraction of N_2 can be calculated as $c_{N_2} = 1 - (c_{He} + c_{O_2})$. Figure 23 compares the average reconstruction errors among the GPLVMs with various kernels and the POD-based predictive model for static temperature and helium mass fraction. It shows similar tendencies to those of the axisymmetric intakes in Fig. 10, and the GPLVMs can offer more accurate dimensionally reduction than POD except for GPLVM with the linear kernel. As with the case of axisymmetric intakes, the exponential kernel has achieved accurate dimensionality reduction, again indicating its suitability for the ROM of supersonic/hypersonic flowfields.

Figure 24 also compares the average reconstruction errors between GPLVM with the exponential kernel and POD for the other flow properties, indicative of more accurate reconstruction achieved by GPLVM than POD.

The prediction accuracy is compared in Fig. 25, which shows higher prediction accuracy of GPLVMs than POD as well, while the Matern52 kernel has shown slightly better performance than the exponential and Matern32 kernels. Figure 26 compares the prediction

TABLE VIII. Correlation between uncertainty in reconstruction and prediction errors for GPLVM with exponential kernel (intake).

	MAE	MSE	RMSE	MAPE	RMSPE
T	0.7919	0.6917	0.7836	0.7572	0.7417
p	0.8514	0.6821	0.7791	0.1615	0.2371
u	0.7111	0.6848	0.7716	0.9017	0.9016
v	0.6733	0.6042	0.6944	0.5290	0.4656

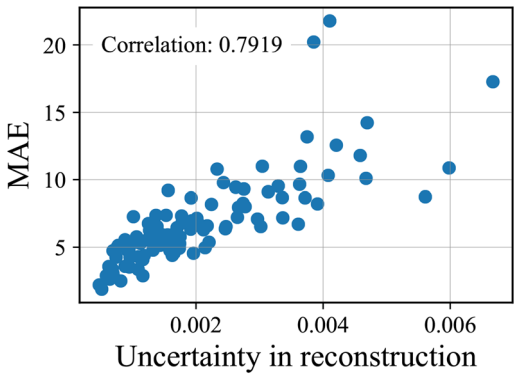

FIG. 17. Relation between uncertainty and prediction MAE for static temperature (intake).

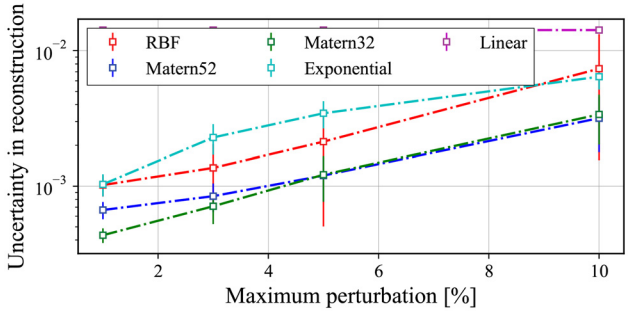

FIG. 18. Relation between uncertainty in reconstruction and uncertainty in latent variables for static temperature (intake).

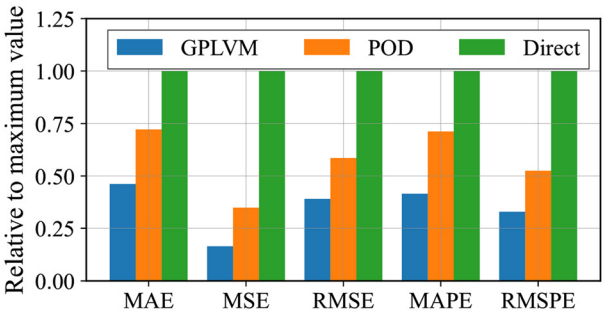

(a) Static temperature

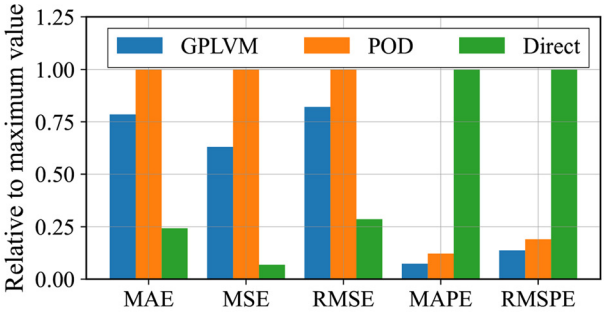

(b) Static pressure

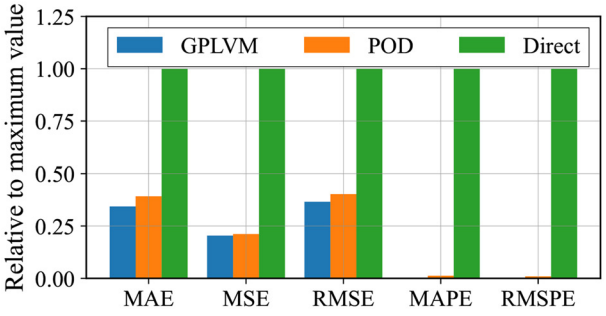

(c) Axial velocity component

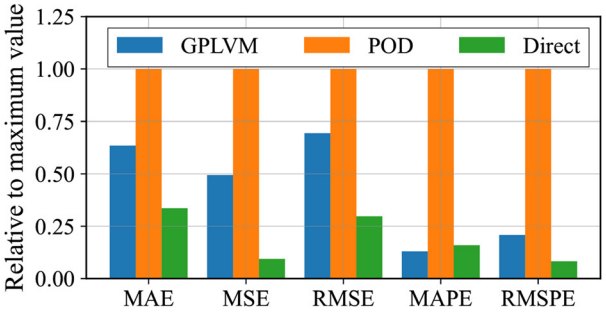

(d) Radial velocity component

FIG. 19. Comparison of prediction errors among GPLVM-based, POD-based, and direct prediction models (intake).

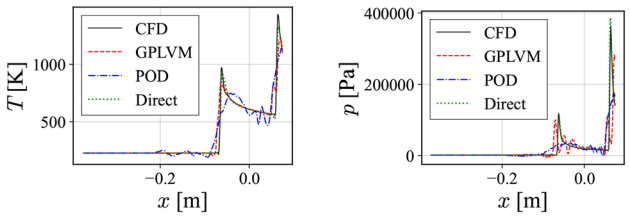

(a) Static temperature (b) Static pressure

FIG. 20. Comparison of centerline static temperature and static pressure distributions among different models (intake, ID 37).

errors between GPLVM with the exponential kernel and POD, while the other metrics are compared in Table IX for all targeted flow properties. The prediction errors are small for all metrics for GPLVM, demonstrating the capability of the GPLVM-based predictive models to predict fuel mixing flowfields accurately.

Figure 27 compares the predicted flowfields via GPLVM with the exponential kernel with the actual (CFD) flowfields, and the absolute error distributions for static temperature and helium mass fraction are shown in Figs. 28 and 29, respectively. The displayed cases have the median MAE (ID 32) and the largest MAE (ID 15) for static temperature and the median MAE (ID 66) and the largest MAE (ID 49) for helium mass fraction. The regions where the phenomena relevant to fuel injection occur are enlarged to facilitate investigation. Accurate flow prediction has been achieved for both static temperature and helium mass fraction, as seen in Fig. 27. Relatively large errors are observed in the vicinity of the shock waves for static temperature in Fig. 28. On the other hand, prediction accuracy has deteriorated only around the mixing layer in the case of helium mass fraction (Fig. 29). Relatively large prediction errors for static temperature have also been observed near shock waves in intakes in Fig. 15. On the other hand, relatively large prediction errors near shock waves (particularly separation and bow shocks) have not been observed for chemical species (Fig. 29). This is because the distributions of chemical species are not largely affected by the difference in such regions and the mass fractions of chemical species are not affected by shock waves due to the nature of frozen flow. Relatively large prediction errors of mass fractions occur in the regions where a fair amount of injected species exists because the mass fraction distributions of chemical species vary only in these regions.

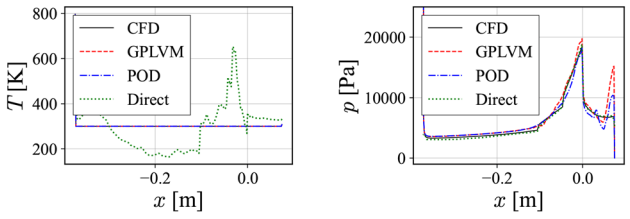

(a) Static temperature (b) Static pressure

FIG. 21. Comparison of surface static temperature and static pressure distributions among different models (intake, ID 37).

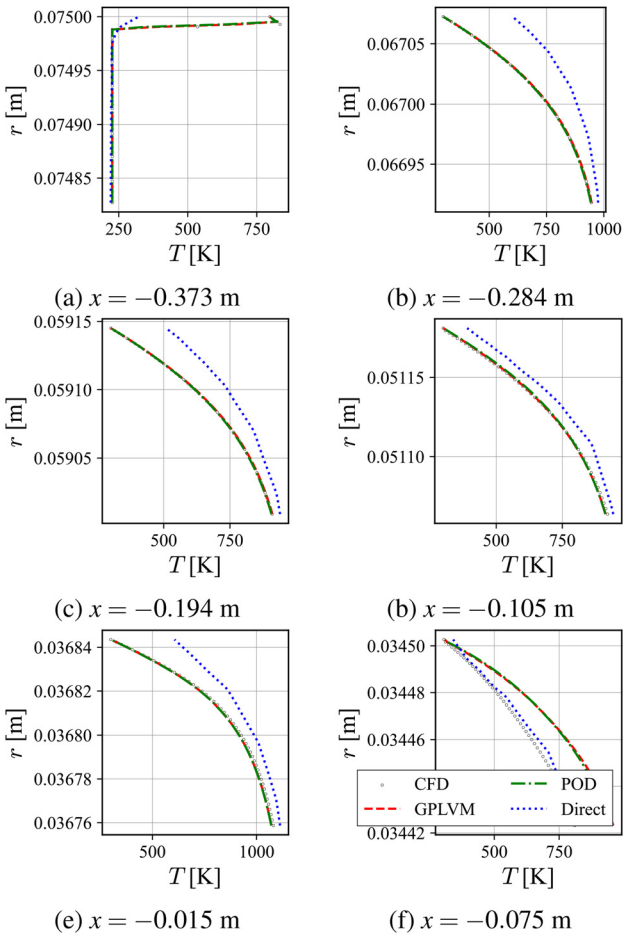

FIG. 22. Comparison of static temperature distributions in vicinity of intake surface (ID 37).

Figure 30 shows the distributions of absolute errors for the other flow properties. In the case of static pressure and velocity components, the distributions are shown for ID 32, whereas the oxygen mass fraction distribution is shown for ID 66, which corresponds to the cases with the median absolute errors for static temperature and helium mass fraction, respectively. All targeted flow properties have been predicted with reasonable accuracy, as indicated by small prediction errors. The error distributions of static pressure and velocity components are similar to that of static temperature [Fig. 28(a)] while that of oxygen mass fraction is akin to that of helium mass fraction [Fig. 29(a)].

2. Uncertainty quantification

The uncertainty associated with the prediction of injection flowfields has been quantified and the results have been summarized in the form of correlation coefficients between uncertainty and error measurements in Table X, showing a strong correlation between uncertainty in reconstruction and the prediction errors. The observed tendencies of the correlation coefficients are similar to those observed in the case of the axisymmetric intakes in Table VIII. The mass

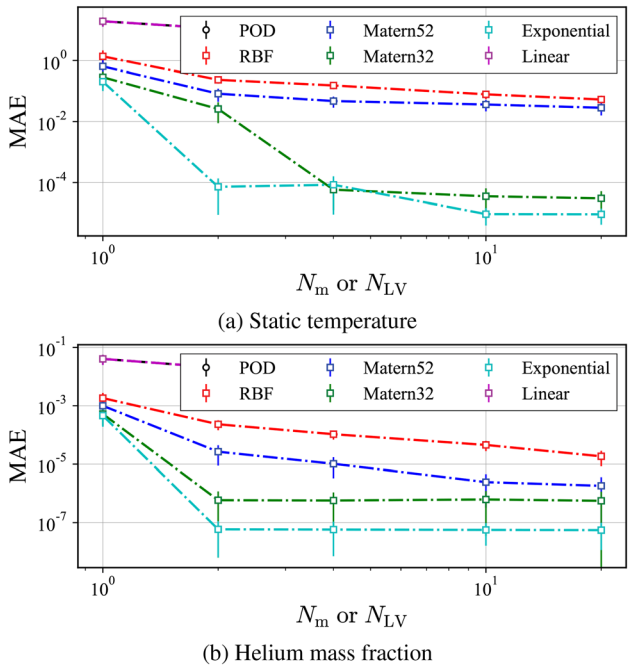

FIG. 23. Comparison of average reconstruction MAEs among GPLVMs with different kernels and POD (fuel injection).

fractions of chemical species (c_{He} and c_{O_2}) are characterized by large values of correlation coefficients.

Distributions of uncertainties obtained via GPLVM with the predicted latent variables are displayed in the design space in Fig. 31, with the training data denoted by white circles. The uncertainties are found to increase in the region where training data are rather sparse such as near the corners of the design space.

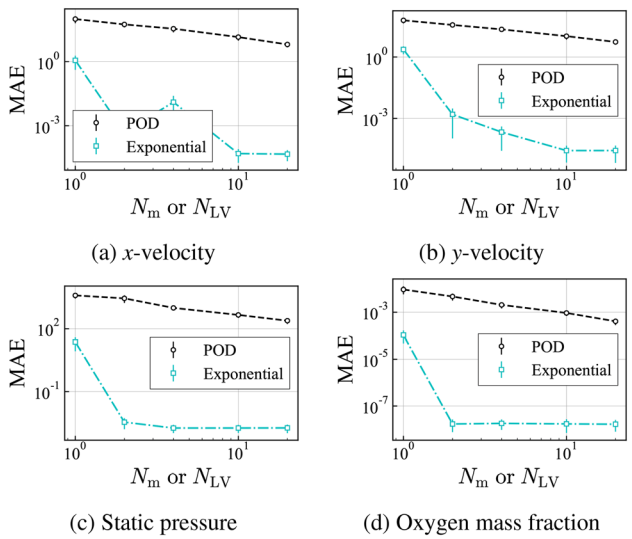

FIG. 24. Comparison of average reconstruction MAEs between GPLVM and POD for other flow properties (fuel injection).

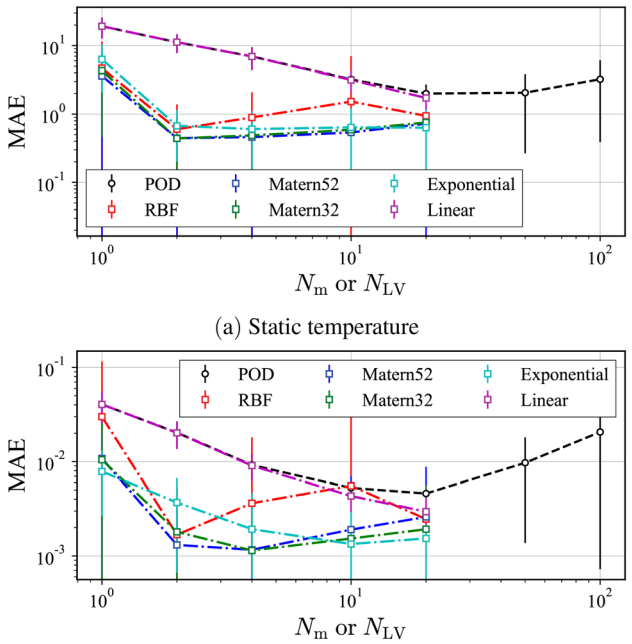

FIG. 25. Comparison of average prediction MAEs among GPLVMs with different kernels and POD (fuel injection).

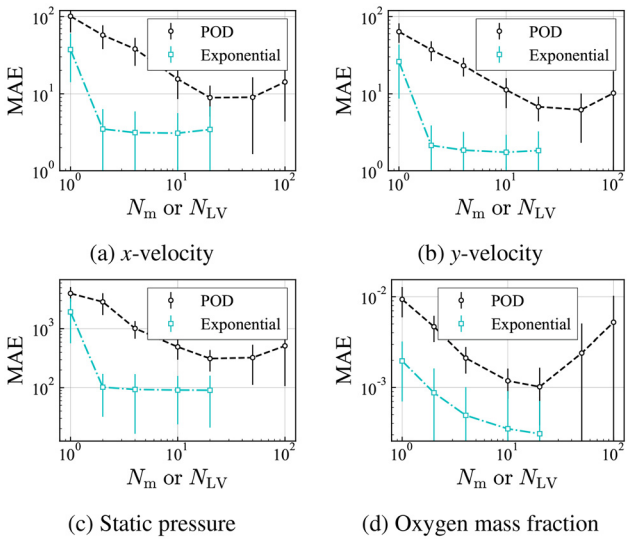

FIG. 26. Comparison of average prediction MAEs between GPLVM and POD for other flow properties (fuel injection).

A region with large uncertainty is present around 1.5×10^5 Pa of injection pressure and 80° of injection angle in helium mass fraction [Fig. 31(b)]. To prove into the factors that account for this large uncertainty, the distributions of helium mass fraction are displayed in Fig. 32 for two cases (IDs 239 and 14) sampled from this region. A relatively small helium mass fraction distribution is observed downstream of the injection in the case of ID 239, while no such distributions are found for ID 14. Figure 33 displays the distributions of latent variables for the training data. An isolated distribution of the latent variables can be seen for helium mass fraction for ID 239 [Fig. 33(b)], while such distributions are not found for static temperature [Fig. 33(a)], consistent with the observation in Fig. 31. It follows that uncommon flowfields that have unusual distributions of flow variables are also characterized by unusual distributions of latent variables in the ROM via GPLVM. In addition, the predictive part (MLP) may give rise to larger prediction errors than usual for such cases, consequently resulting in such large uncertainties. These results are indicative of the utility of this characteristic to detect anomalies in the training dataset by scrutinizing the values of latent variables, while further investigation is required to enable nonintrusive anomaly detection without losing important characteristics of the dataset.

3. Comparison with direct model

The prediction errors among the three prediction models for static temperature and helium mass fraction are compared in a relative

TABLE IX. Comparison of average prediction errors between GPLVM with exponential kernel and POD (fuel injection).

	Model	MAE	MSE	RMSE	MAPE	RMSPE
T	GPLVM	0.604	4.71	1.69	4.5×10^{-3}	0.0170
	POD	2.00	19.5	4.21	0.0168	0.0496
p	GPLVM	90.7	1.3×10^5	308	6.6×10^{-3}	0.0399
	POD	314	5.5×10^5	707	0.0300	0.164
V_x	GPLVM	3.08	143	8.22	24.5	483
	POD	8.93	447	18.7	1.4×10^3	2.7×10^4
V_y	GPLVM	1.74	56.7	6.52	32.3	933
	POD	6.79	314	17.2	737	2.5×10^4
c_{O_2}	GPLVM	1.3×10^{-3}	4.3×10^{-5}	4.3×10^{-3}	7.91	16.5
	POD	4.6×10^{-3}	6.7×10^{-5}	7.6×10^{-3}	102	169
c_{He}	GPLVM	1.3×10^{-4}	1.9×10^{-6}	1.0×10^{-3}	5.48	22.2
	POD	1.0×10^{-3}	3.4×10^{-6}	1.7×10^{-3}	29.8	73.5

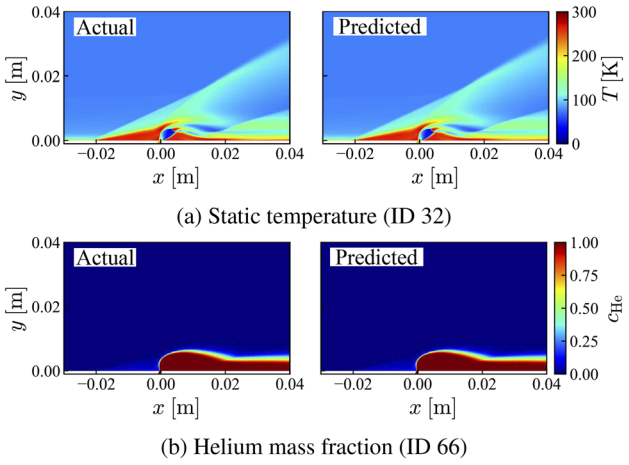

(a) Static temperature (ID 32)

(b) Helium mass fraction (ID 66)

FIG. 27. Comparison between predicted (GPLVM) and actual (CFD) flowfields of injection.

manner in Fig. 34. For both static temperature and helium mass fraction, GPVLM with the exponential kernel has achieved the most accurate prediction among these three models, while the accuracy of the prediction via GPVLM is comparable to that of the direct model in the case of axisymmetric intake flowfields in Fig. 19. It is deduced that GPVLM is applicable to the prediction of various supersonic/hypersonic flowfields with reasonable accuracy, while the adaptability varies depending on the characteristics of the dataset or target flowfields. The results of static pressure and velocity components are similar to that of

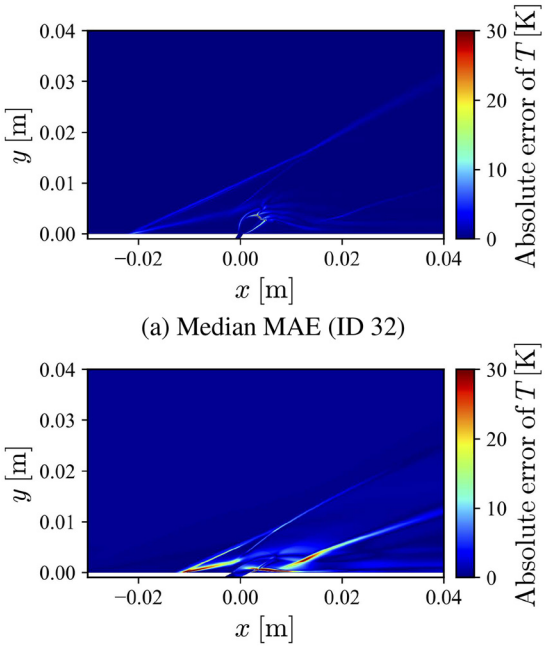

(a) Median MAE (ID 32)

(b) Largest MAE (ID 15)

FIG. 28. Distributions of absolute errors of static temperature in injection flowfields.

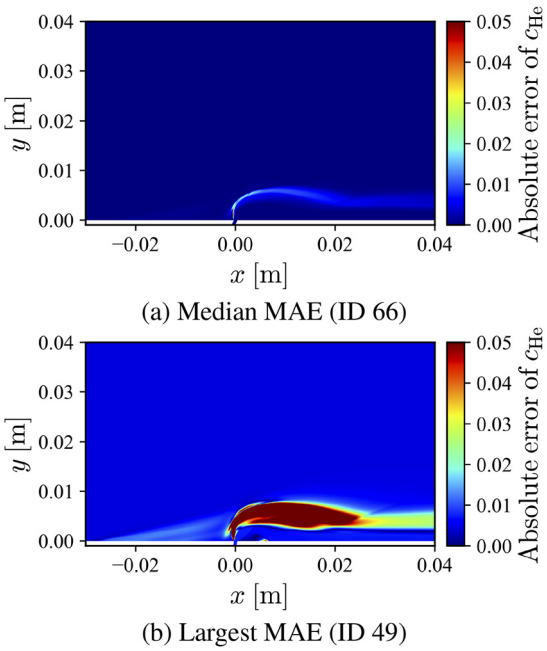

(a) Median MAE (ID 66)

(b) Largest MAE (ID 49)

FIG. 29. Distributions of absolute errors of helium mass fraction in injection flowfields.

static temperature, while oxygen mass fraction has the same trend as helium mass fraction.

Static temperature distributions in the vicinity of the bottom wall are shown in Fig. 35. It can be seen that GPLVM can predict thermal boundary layer accurately, while direct prediction has relatively large prediction errors, as is consistent with the results of axisymmetric intake flowfields (Fig. 22). Figure 36 displays the predicted distributions of static temperature and static pressure on the bottom wall from different models. While GPLVM and POD predicted the distributions precisely, the direct prediction again incurred relatively large errors. These results indicate that the ROM-based methods can commonly predict flow structures such as the boundary layers and freestream accurately, because the flow structures do not vary significantly even with the variations in design variables and latent variables.

IV. DISCUSSION

A. Influence of kernels

In GPLVM-based predictive modeling, the selection of kernels has been found to have significant impact on prediction performance and characteristics. The selection criteria of favorable kernels for the prediction of supersonic/hypersonic flowfields are discussed in the present section. For both axisymmetric intake and two-dimensional fuel injection cases, the exponential kernel achieved high prediction accuracy, while the RBF kernel resulted in the largest reconstruction errors and large prediction errors. The linear kernel, on the other hand, showed similar characteristics to POD-based ROM and prediction. The distributions of relative prediction errors in static temperature are compared among GPLVM-based predictive models with different kernels in Fig. 37. A characteristic difference can be observed in the error distributions around the centerline shock reflection.

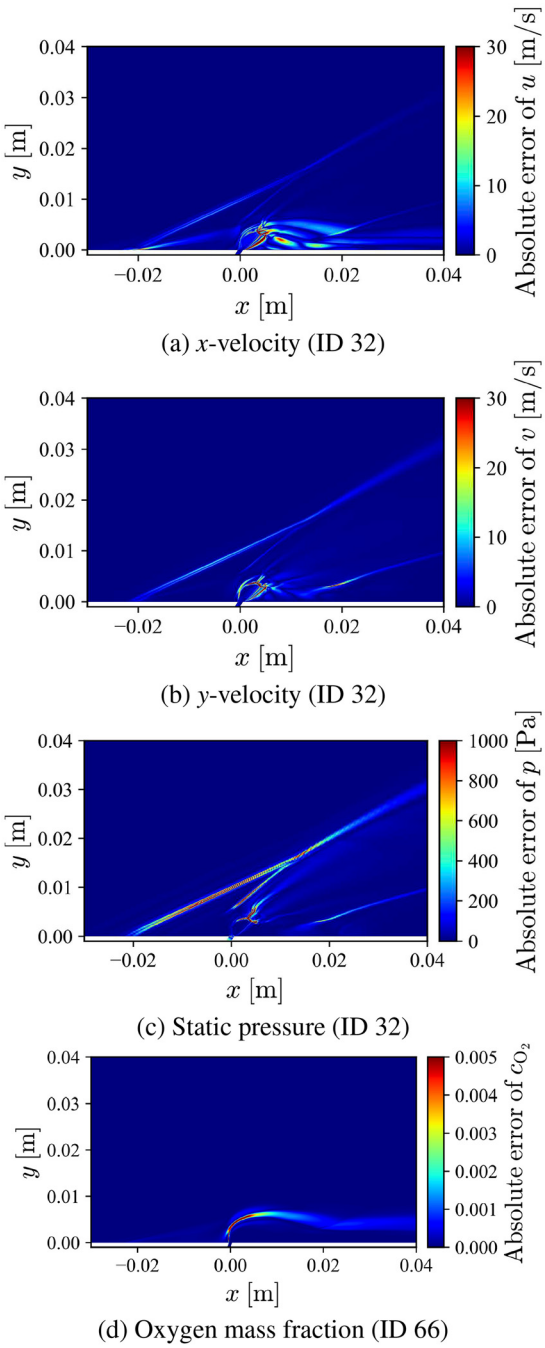

FIG. 30. Absolute error distributions in injection flowfields for other flow properties.

While the errors in centerline distributions are present only in the vicinity of the shock reflection for the exponential kernel, those of the linear kernel are characterized by a wider spread than the others. Detailed comparison is made with respect to the centerline static temperature distributions in Fig. 38.

TABLE X. Correlation coefficients between uncertainty in reconstruction and prediction errors for GPLVM with exponential kernel (fuel injection).

	MAE	MSE	RMSE	MAPE	RMSPE
T	0.7604	0.6128	0.7253	0.7554	0.6062
p	0.7294	0.6699	0.6699	0.6709	0.3312
V_x	0.6502	0.4895	0.6261	0.8103	0.8107
V_y	0.8203	0.7542	0.7982	0.6297	0.3223
c_{He}	0.9514	0.9056	0.9009	0.9544	0.9034
c_{O_2}	0.9416	0.8701	0.8675	0.8718	0.8393

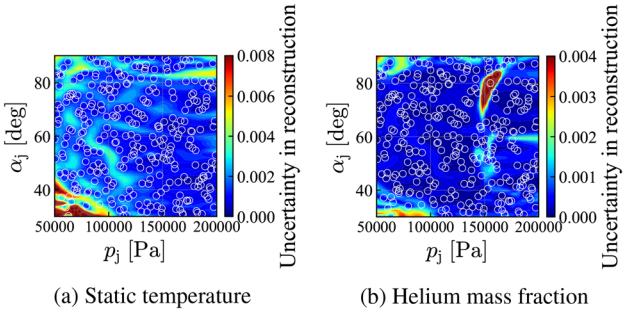

FIG. 31. Distributions of uncertainty in reconstruction (fuel injection).

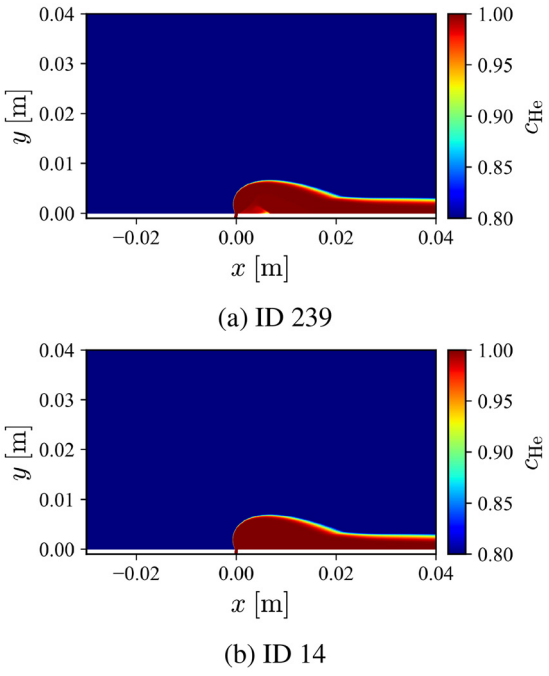

FIG. 32. Helium mass fraction distributions from CFD.

The difference observed above can be explained by different characteristics of the kernels. In GPLVM, the kernel plays a role in weighting the training data based on the similarity with the prediction inputs. Figure 39 graphically illustrates the weights for all training data

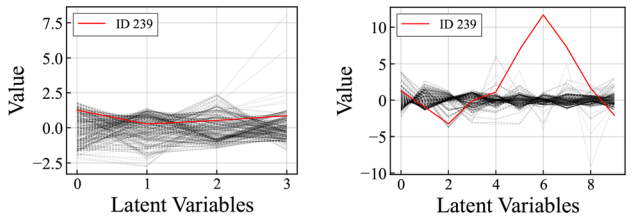

(a) Static temperature (b) Helium mass fraction

FIG. 33. Distributions of latent variables for training dataset (fuel injection).

to reconstruct the output that corresponds to the given input for each kernel. Darker color represents larger weights. In the case of smooth kernels like the RBF kernel [Fig. 39(a)], a relatively large number of training data are used to reconstruct outputs, resulting in less sharp shock waves in predicted flowfields. GPLVM with the linear kernel and POD use all training data for prediction or reconstruction [Fig. 39(c)], resulting in more blurred shock waves in predicted flowfields. The exponential kernel, which is relatively non-smooth function on the other hand, refers to fewer training data for prediction [Fig. 39(b)]. This is deemed to account for a relatively accurate and crisp prediction of shock waves for this model.

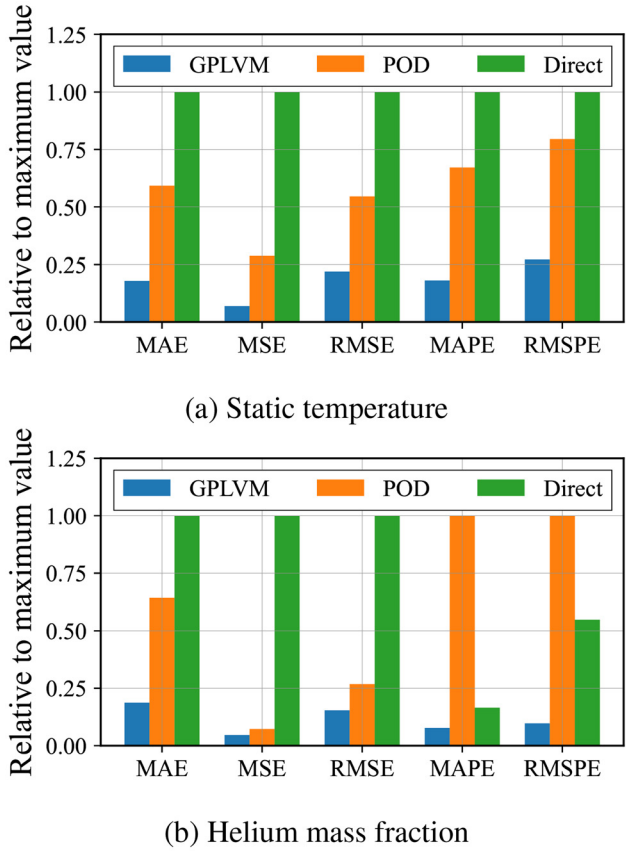

(a) Static temperature

(b) Helium mass fraction

FIG. 34. Comparison of prediction errors among all models (fuel injection).

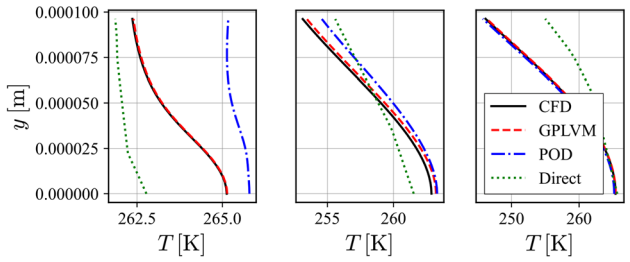

(a) $x = -0.01$ m (b) $x = 0.01$ m (b) $x = 0.03$ m

FIG. 35. Comparison of static temperature profiles (fuel injection, ID 32).

As discussed here, the selection of the kernel has been found to have influence on the outputs hence accuracy of prediction to some extent, while most of the kernels considered have yielded superior performance to the POD-based approach. Although the present study has employed a commonly used kernel for each model, it may help to improve its performance to use multiple kernels in combination or design new kernels optimized for each flow prediction problem.

B. Characteristics of GPLVM-based predictive modeling

The characteristics of predictive modeling are compared among GPLVM-based, POD-based, and direct approaches in Table XI, where the symbols denote favorable/possible (◯), fair/possible with some modification (△), and unfavorable/difficult (×) characteristics. Comparison is made with respect to five criteria to allow for effective selection of prediction approaches including (a) prediction accuracy, (b) computational cost, (c) availability of uncertainty quantification, (d) capability of multivariate prediction, and (e) applicable computational mesh type.

GPLVM-based and direct prediction approaches offer accurate prediction with different characteristics, whereas the POD-based approach is inferior to the other approaches for the case of axisymmetric intakes, as discussed in Sec. III A 3. The proposed GPLVM-based approach has also yielded the highest accuracy in the case of two-dimensional injection flowfields, as presented in Sec. III B 3. For all models, further improvement can be made by tuning the hyperparameters of the deep-learning models. In the case of GPLVM, the use of different kernels can alter the prediction accuracy, and the selection of suitable kernels therefore may allow the proposed framework to

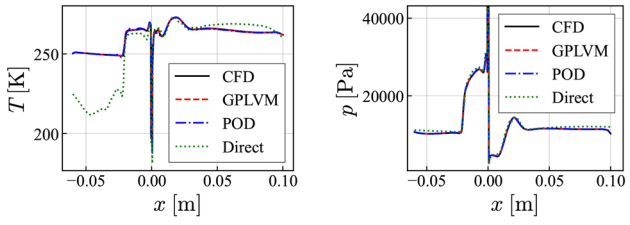

(a) Static temperature (b) Static pressure

FIG. 36. Comparison of wall pressure distributions among different models (fuel injection, ID 32).

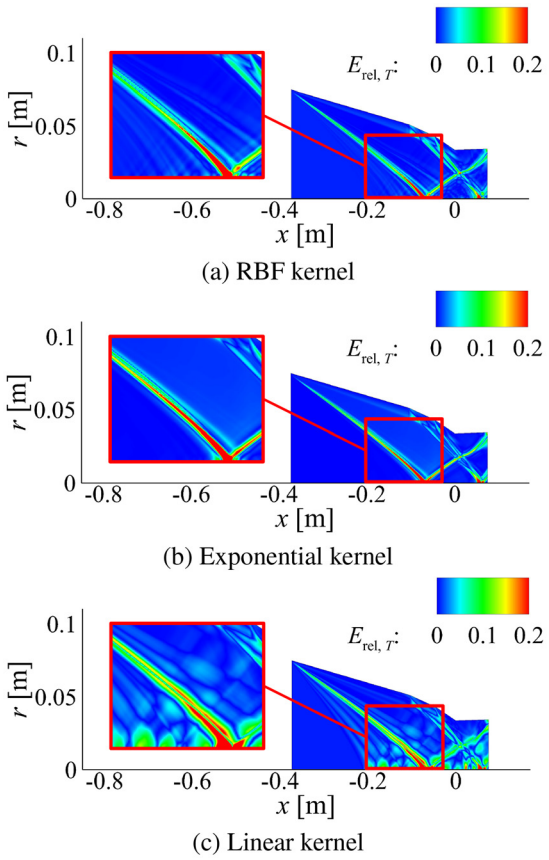

FIG. 37. Comparison of prediction error distributions in intake flowfields among GPLVM-based predictive models with different kernels.

provide flexible applicability for various problems, while such flexibility of deep learning has already been recognized.[14]

The computational cost of ROM-based approaches consists of those for ROM and predictive modeling. GPLVM requires a computational cost for gradient-based optimization of latent variables and kernel hyperparameters and POD requires one for singular value decomposition (SVD), while the costs of predictive modeling are the same between these two approaches in the present study. The computational time for modeling is summarized in Table XII for the axisymmetric intake problem. It indicates that the computational time for the ROM part is much smaller than that for the MLP part.

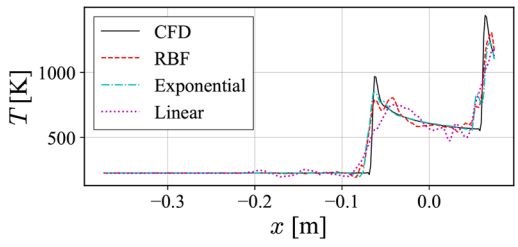

FIG. 38. Comparison of centerline static temperature distributions of intake flowfields among GPLVM-based predictive models with different kernels.

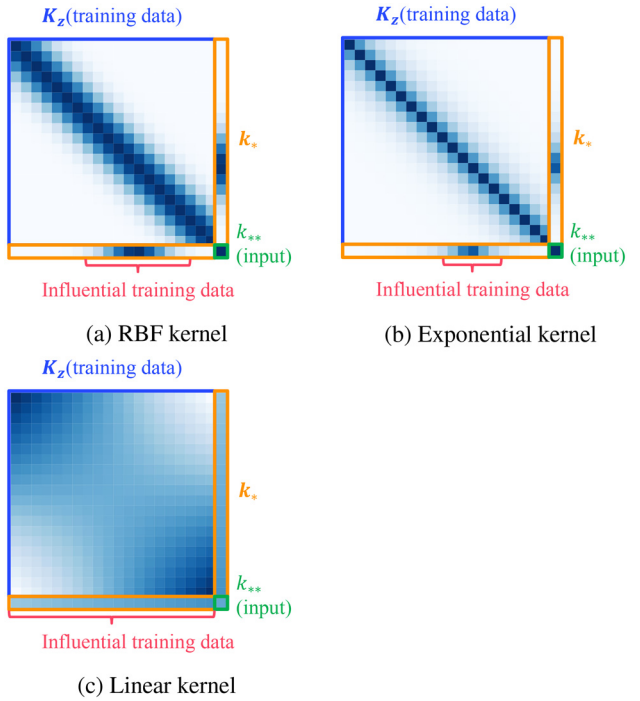

FIG. 39. Characteristics of kernels in data reconstruction in GPLVM.

TABLE XI. Comparison of characteristics of three predictive modeling approaches (◯: favorable/possible, △: fair/possible with some modification, ×: unfavorable/difficult).

	GPLVM	POD	Direct
Prediction accuracy	◯	△	◯
Computational cost	◯	◯	△
Uncertainty quantification	◯	×	△
Multivariate prediction	△	×	◯
Applicable mesh type	Structured	Structured	Any

The computational time for the MLP part largely depends on the number of training epochs, which varies between ROM-based models (POD and GPLVM) and the direct model, i.e., 10 000 and 250, respectively. The number of epochs can be reduced by adjusting the setups of hyperparameters. The direct prediction model usually requires much larger computational cost than the others, while it can be reduced by the acceleration via graphics processing units (GPUs).

TABLE XII. Comparison of computational time for training among three models (intake).

	ROM part (h)	MLP part (h)	Total (h)
GPLVM	0.2	19.5	19.7
POD	0.0	19.5	19.5
Direct	···	297.2	297.2

Uncertainty quantification (UQ) is a key technique to increase and assure the reliability of prediction. Furthermore, UQ helps to improve the model accuracy by indicating the data that should be added to the existing dataset. As discussed in Secs. III A 2 and III B 2, GPLVM is capable of UQ without requiring any additional treatments due to its stochastic characteristic. UQ for the direct model is reported by using the Monte Carlo Dropout and ensemble of prediction.[26] However, the approach inherently requires additional model training processes, which inevitably incur additional computational costs, and tuning may well be required for the Dropout rate which determines the probability of the Dropout. To our knowledge, there are a few approaches of UQ that are applicable for POD-based approaches.

The capability of multivariate prediction, i.e., the ability to predict multiple flow properties (e.g., static temperature, static pressure, and velocity components) by one model, is a desirable feature because the assessment of performance parameters such as compression efficiency and drag for intakes and mixing efficiency for fuel injection essentially requires the information on multiple flow properties. The direct prediction model can inherently deal with multiple variables in one model, whereas the GPLVM-based and POD-based approaches have difficulty in predicting multiple properties. To enable multivariate prediction via GPLVM, shared GPLVM has been proposed by Ek[49] and this can be adopted as the extension of the proposed predictive modeling.

As regards suitable mesh types, GPVLM-based and POD-based modeling approaches are difficult to apply to datasets with unstructured grids because they require a consistent and specific allocation of computational nodes or cells. On the other hand, the direct approach does not specify the mesh type of datasets or even the number of nodes in each data. It can thus be reasonably concluded that the proposed GPLVM-based predictive framework is more efficient and reliable due to its sufficiently high accuracy with low computational cost as well as its capability of uncertainty quantification.

V. CONCLUSIONS

The present study has proposed a new ROM-based predictive framework of supersonic/hypersonic flowfields using a Gaussian process latent variable model (GPLVM) in conjunction with deep learning. GPLVM is employed for dimensionality reduction of the flowfield dataset into an arbitrarily small number of latent variables. The prediction of flowfields is then achieved by predicting the latent variables via deep learning which employs the design variables as inputs. The present study employs GPLVM for two reasons, namely, (1) GPLVM is a ROM technique itself while conventional ROM techniques in flow prediction often employ decomposition techniques subject to loss of information on the dataset and (2) the stochastic characteristic of GPLVM allows for uncertainty quantification in prediction. The capability and applicability have been assessed for axisymmetric supersonic intake flowfields and two-dimensional fuel injection flowfields.

The capability of GPLVM as a ROM technique has been investigated by comparison to POD for the same number of latent variables or modes. GPLVM has been found to offer dimensionality reduction with smaller reconstruction errors and hence loss of information for all kernels except for the linear kernel. Efficient ROMs have resulted in more accurate prediction than POD-based predictive modeling as well as direct prediction while the computational cost is comparable to that of POD-based prediction and significantly smaller than that of direct prediction via deep learning. Furthermore, uncertainty quantification is available in the case of GPLVM owing to its characteristic as a stochastic process, which allows for effective use of prediction, whereas the POD-based prediction model does not offer such capability and direct prediction requires further computational cost for it. In terms of both accuracy and reliability, GPLVM-based predictive modeling offers advantages over POD-based and direct predictive modeling approaches at reasonable computational cost for modeling.

Scrutinization of the prediction outputs has revealed that the selection of kernel has considerable influence on the predicted flowfields, signifying the possibility of favorable selection of kernels for supersonic/hypersonic flowfields. In particular, shock waves in predicted flowfields have been affected considerably by the difference in the kernel. It has been found that smooth kernels such as RBF (Gaussian) and Matern52 are not suitable while the exponential kernel characterized by a relatively pronounced function allows for sharper prediction of shock waves, which cannot be achieved by POD. Direct prediction via deep learning has been found to realize sharp prediction of shock waves owing to its capability to fit highly nonlinear or discontinuous distributions, while the prediction accuracy in near-wall regions has been deteriorated.

The present predictive framework has demonstrated its capabilities of accurate prediction and uncertainty quantification in supersonic/hypersonic flowfields in scramjet engines. While further investigation is required to examine the applicability of the present approach for wider ranges of flow regimes, GPLVM-based flow prediction represents a promising alternate for fast, accurate, and reliable predictive modeling for supersonic and hypersonic flowfields.

ACKNOWLEDGMENTS

The authors acknowledge the support provided by the Japan Society for the Promotion of Science (JSPS) through the KAKENHI (Grant No. 17K20144) and the Grant-in-Aid for JSPS Fellows (Grant No. 22J20613) as well as the Japan Science and Technology Agency through the JST SPRING (Grant No. JPMJSP2136).

AUTHOR DECLARATIONS

Conflict of Interest

The authors have no conflicts to disclose.

Author Contributions

Chihiro Fujio: Conceptualization (equal); Data curation (equal); Formal analysis (equal); Funding acquisition (equal); Investigation (lead); Methodology (lead); Project administration (equal); Validation (lead); Visualization (lead); Writing – original draft (lead); Writing – review & editing (supporting). **Kento Akiyama:** Data curation (equal); Formal analysis (equal); Investigation (equal); Methodology (equal); Validation (equal); Visualization (equal); Writing – original draft (equal). **Hideaki Ogawa:** Funding acquisition (lead); Investigation (supporting); Project administration (lead); Supervision (lead); Writing – review & editing (equal).

DATA AVAILABILITY

The data that support the findings of this study are available from the corresponding author upon reasonable request.

REFERENCES

[1]C. R. McClinton, "X-43—Scmanjet power breaks the hypersonic barrier Dryden lectureship in research for 2006," AIAA Paper No. AIAA 2006-1, 2006.
[2]P. Klink and H. Ogawa, "Investigation on the performance and feasibility of RBCC-based access-to-space via multi-objective design optimization," Acta Astronaut. **157**, 435–454 (2019).
[3]M. K. Smart, N. E. Hass, and A. Paull, "Flight data analysis of the HyShot 2 scramjet flight experiment," AIAA J. **44**, 2366–2375 (2006).
[4]H. Ogawa and R. R. Boyce, "Physical insight into scramjet inlet behavior via multi-objective design optimization," AIAA J. **50**, 1773–1783 (2012).
[5]C. Fujio and H. Ogawa, "Physical insight into axisymmetric scramjet intake design via multi-objective design optimization using surrogate-assisted evolutionary algorithms," Aerosp. Sci. Technol. **113**, 106676 (2021).
[6]S. Brahmachary, C. Fujio, M. Aksay, and H. Ogawa, "Design optimization and off-design performance analysis of axisymmetric scramjet intakes for ascent flight," Phys. Fluids **34**, 036109 (2022).
[7]W. Huang, J. Yang, and L. Yan, "Multi-objective design optimization of the transverse gaseous jet in supersonic flows," Acta Astronaut. **93**, 13–22 (2014).
[8]H. Ogawa, "Physical insight into fuel-air mixing for upstream-fuel-injected scramjets via multi-objective design optimization," J. Propul. Power **31**, 1505–1523 (2015).
[9]H. Ogawa, R. R. Boyce, A. Isaacs, and T. Ray, "Multi-objective design optimisation of inlet and combustor for axisymmetric scramjets," Open Thermodyn. J. **4**, 86–91 (2010).
[10]S. Kumar, S. Das, and S. Sheelam, "Application of CFD and the Kriging method for optimizing the performance of a generic scramjet combustor," Acta Astronaut. **101**, 111–119 (2014).
[11]H. Ogawa and R. R. Boyce, "Nozzle design optimization for axisymmetric scramjets by using surrogate-assisted evolutionary algorithms," J. Propul. Power **28**, 1324–1338 (2012).
[12]S. Ju, C. Yan, X. Wang, Y. Qin, and Z. Ye, "Optimization design of energy deposition on single expansion ramp nozzle," Acta Astronaut. **140**, 351–361 (2017).
[13]C. Fujio and H. Ogawa, "Physical insights into multi-point global optimum design of scramjet intakes for ascent flight," Acta Astronaut. **194**, 59–75 (2022).
[14]S. L. Brunton, B. R. Noack, and P. Koumoutsakos, "Machine learning for fluid mechanics," Annu. Rev. Fluid Mech. **52**, 477–508 (2020).
[15]L. J. Lumiley, "The structure of inhomogeneous turbulent flows," *Atmospheric Turbulence Radio Wave Propagation* (Nauka, 1967), pp. 166–178.
[16]P. J. Schmid, "Dynamic mode decomposition of numerical and experimental data," J. Fluid Mech. **656**, 5–28 (2010).
[17]K. Taira, S. L. Brunton, S. T. Dawson, C. W. Rowley, T. Colonius, B. J. McKeon, O. T. Schmidt, S. Gordeyev, V. Theofilis, and L. S. Ukeiley, "Modal analysis of fluid flows: An overview," AIAA J. **55**, 4013–4041 (2017).
[18]C. W. Rowley and S. T. Dawson, "Model reduction for flow analysis and control," Annu. Rev. Fluid Mech. **49**, 387–417 (2017).
[19]K. Taira, M. S. Hemati, S. L. Brunton, Y. Sun, K. Duraisamy, S. Bagheri, S. T. Dawson, and C. A. Yeh, "Modal analysis of fluid flows: Applications and outlook," AIAA J. **58**, 998–1022 (2020).
[20]T. Bui-Thanh, M. Damodaran, and K. Willcox, "Aerodynamic data reconstruction and inverse design using proper orthogonal decomposition," AIAA J. **42**, 1505–1516 (2004).
[21]M. Mifsud, S. Shaw, and D. MacManus, "A high-fidelity low-cost aerodynamic model using proper orthogonal decomposition," Int. J. Numer. Methods Fluids **63**, 494 (2009).
[22]J. Yu and J. S. Hesthaven, "Flowfield reconstruction method using artificial neural network," AIAA J. **57**, 482–498 (2019).
[23]X. Wang, J. Kou, and W. Zhang, "Multi-fidelity surrogate reduced-order modeling of steady flow estimation," Int. J. Numer. Methods Fluids **92**, 1826–1844 (2020).
[24]F. Sun, W. Y. Su, M. Y. Wang, and R. J. Wang, "RBF-POD reduced-order modeling of flow field in the curved shock compression inlet," Acta Astronaut. **185**, 25–36 (2021).
[25]S. Brahmachary, A. Bhagyarajan, and H. Ogawa, "Fast estimation of internal flowfields in scramjet intakes via reduced-order modeling and machine learning," Phys. Fluids **33**, 106110 (2021).
[26]C. Fujio and H. Ogawa, "Deep-learning prediction and uncertainty quantification for scramjet intake flowfields," Aerosp. Sci. Technol. **130**, 107931 (2022).
[27]K. Akiyama and H. Ogawa, "Fast prediction of two-dimensional flowfields with fuel injection into supersonic crossflow via deep learning," Trans. Jpn. Soc. Aeronaut. Space Sci. (to be published).
[28]C. Kong, J. Chang, Y. Li, and Z. Wang, "A deep learning approach for the velocity field prediction in a scramjet isolator," Phys. Fluids **33**, 026103 (2021).
[29]H. Chen, M. Guo, Y. Tian, J. Le, H. Zhang, and F. Zhong, "Intelligent reconstruction of the flow field in a supersonic combustor based on deep learning," Phys. Fluids **34**, 035128 (2022).
[30]Y. Li, J. Chang, Z. Wang, and C. Kong, "An efficient deep learning framework to reconstruct the flow field sequences of the supersonic cascade channel," Phys. Fluids **33**, 056106 (2021).
[31]X. Deng, M. Guo, H. Chen, Y. Tian, J. Le, and H. Zhang, "Dual-path flow field reconstruction for a scramjet combustor based on deep learning," Phys. Fluids **34**, 095118 (2022).
[32]Y. Li, J. Chang, C. Kong, and W. Bao, "Recent progress of machine learning in flow modeling and active flow control," Chin. J. Aeronaut. **35**, 14–44 (2022).
[33]C. Qiu, Q. Huang, G. Pan, and X. He, "Framework for a variational Bayesian convolutional network for velocity field prediction and uncertainty quantification of a pump-jet propulsor," Phys. Fluids **34**, 077109 (2022).
[34]N. Thuerey, K. Weißenow, L. Prantl, and X. Hu, "Deep learning methods for Reynolds-averaged Navier–Stokes simulations of airfoil flows," AIAA J. **58**, 25–36 (2020).
[35]N. Lawrence, "Probabilistic non-linear principal component analysis with Gaussian process latent variable models," J. Mach. Learn. Res. **6**(60), 1783–1816 (2005); available at http://jmlr.org/papers/v6/lawrence05a.html
[36]S. Nakaya, K. Omi, T. Okamoto, Y. Ikeda, C. Zhao, M. Tsue, and H. Taguchi, "Instability and mode transition analysis of a hydrogen-rich combustion in a model afterburner," Proc. Combust. Inst. **38**, 5933–5942 (2021).
[37]S. Nishimoto, S. Nakaya, J. Lee, and M. Tsue, "Effects of the penetration height of ethylene transverse jets on flame stabilization behavior in a Mach 2 supersonic crossflow," Proc. Combust. Inst. (published online, 2023).
[38]D. C. Liu and J. Nocedal, "On the limited memory BFGS method for large scale optimization," Math. Program. **45**, 503–528 (1989).
[39]GPy, "GPy: A Gaussian process framework in python," https://github.com/SheffieldML/GPy (2014).
[40]M. Abadi, P. Barham, J. Chen, Z. Chen, A. Davis, J. Dean, M. Devin, S. Ghemawat, G. Irving, M. Isard, M. Kudlur, J. Levenberg, R. Monga, S. Moore, D. G. Murray, B. Steiner, P. Tucker, V. Vasudevan, P. Warden, M. Wicke, Y. Yu, and X. Zheng, "TensorFlow: A system for large-scale machine learning," in *12th USENIX Symposium on Operating Systems Design and Implementation (OSDI 16)* (USENIX Association, Savannah, GA, 2016), pp. 265–283.
[41]D. P. Kingma and J. L. Ba, "Adam: A method for stochastic optimization," in 3rd International Conference on Learning Representations, 2015.
[42]R. R. Boyce, S. C. Tirtey, L. Brown, M. Creagh, and H. Ogawa, "SCRAMSPACE: Scramjet-based Access-to-Space Systems," in 17th AIAA International Space Planes and Hypersonic Systems and Technologies Conference, 2011.
[43]K. Inoue, S. Aso, and S. Kawano, "A study on the effect of fuel injection angle to two-dimensional supersonic mixing for SCRAM-jet engine and PDE," in 54th International Astronautical Congress of the International Astronautical Federation (IAF), the International Academy of Astronautics and the International Institute of Space Law, 2003.
[44]ANSYS, *ANSYS FLUENT User's Guide* (ANSYS Inc., Canonsburg, PA, 2021).
[45]F. R. Menter, "Two-equation eddy-viscosity turbulence models for engineering applications," AIAA J. **32**, 1598 (1994).
[46]C. Geuzaine, "Gmsh: A 3-D finite element mesh generator with built-in pre- and post-processing facilities," Int. J. Numer. Methods Eng. **79**, 1309–1331 (2009).
[47]R. R. Boyce, J. M. Schramm, D. Oberg, K. Hannemann, and L. Brown, "Shock tunnel and numerical studies of a large inlet-fuelled inward turning axisymmetric scramjet," in *18th AIAA/3AF International Space Planes and Hypersonic Systems and Technologies Conference* (AIAA, 2012).
[48]V. Sekar, Q. Jiang, C. Shu, and B. C. Khoo, "Fast flow field prediction over airfoils using deep learning approach," Phys. Fluids **31**, 057103 (2019).
[49]C. H. Ek, "Shared Gaussian process latent variable models," Ph.D. thesis (Oxford Brookes University, 2009).